Flow Visualization of a Turbulent Shear Flow using an
Optical Wavefront Sensor

THESIS

Daniel Warren Jewell
Captain, USAF

AFIT/GEO/ENG/94D-04

DEPARTMENT OF THE AIR FORCE

AIR UNIVERSITY

AIR FORCE INSTITUTE OF TECHNOLOGY

Wright-Patterson Air Force Base, Ohio

AFIT/GEO/ENG/94D-04

Flow Visualization of a Turbulent Shear Flow using an Optical Wavefront Sensor

THESIS
Daniel Warren Jewell
Captain, USAF

AFIT/GEO/ENG/94D-04

Approved for public release; distribution unlimited

AFIT/GEO/ENG/94D-04

Flow Visualization of a Turbulent Shear Flow using an Optical
Wavefront Sensor

THESIS

Presented to the Faculty of the School of Engineering

of the Air Force Institute of Technology

Air University

In Partial Fulfillment of the

Requirements for the Degree of

Master of Science in Electrical Engineering

Daniel Warren Jewell, B.S.

Captain, USAF

December 1994

Preface

I would like to take this opportunity to thank my advisors, Major Mike Rogge-mann and Dr Byron Welsh for their guidance throughout this experimental thesis. I would also like to thank Dr. Bowersox for his assistance in designing the shear-layer turbulence generator that was so important to the success of this research. Most of all, I would like to thank my wife, Shirley, for her unwavering support and love. I would also like to thank my daughters, Pamela and Cathleen, for their understanding when I was at school more often than I was at home.

Daniel Warren Jewell

Table of Contents

List of Figures

List of Tables

Abstract

Many flow visualization techniques have been used to examine turbulent shear flows. Some are intrusive and disrupt the flow, and others require the use of opaque substances that can be photographed. The research reported here investigated the use of a shearing interferometer wavefront sensor to determine the effects of shear-layer turbulence on an optical wavefront. A collimated helium-neon laser beam was propagated through a plane shear-layer produced by mixing helium and nitrogen at different velocities. Since the gases have different indices of refraction, the optical wavefront was distorted by different amounts by each gas. The shearing interferometer (SI) measured the wavefront slope across the sampled area of the wavefront. The slope measurements were then used to reconstruct phase maps showing the shape of the perturbed wavefront. The shear-layer was viewed from the side and the top. This document contains shadowgraphs, interference patterns imaged by each of the shearing interferometer's six cameras, interferograms containing fringes with separation proportional to the wavefront slope in the x and y directions, and phase maps showing the shape of the perturbed optical wavefronts. The results show how an optical wavefront is distorted by shear-layer turbulence. The side view showed an area of steep slope along the mixing area of the two gases. The slope gradually changed as the distance from the mixing layer region increased. For the top view, the peaks and valleys grew as they propagated away from the shear-layer turbulence generator. This indicated that the amount of distortion at a given location would oscillated between a peak and a valley. The results also indicated that the interference patterns recorded by the SI cameras provide a simple way to visualize turbulence in a manner that provides phase information about the wavefront.

Flow Visualization of a Turbulent Shear Flow using an Optical Wavefront Sensor

I. Introduction

1.1 Motivation

The Air Force is investigating the feasibility of using an airborne laser system for defense against theater ballistic missiles. To destroy a missile, the laser beam must remain focused on the fast-moving target and supply enough energy to destroy the target. Since the laser would be mounted in an airplane, the laser beam has to pass through the turbulent air flow that surrounds the airplane in addition to the turbulent atmosphere. The boundary layer causes optical wavefront phase distortions which degrade the optical quality of the laser beam. The turbulence-induced phase distortions reduce the energy density at the target. This loss of energy density would, as a minimum, force the use of a more powerful, expensive, and heavier laser, or, in the worst case, cause the system to fail. Phillips Laboratory, who manages the Airborne Laser (ABL) program, is currently researching ways to compensate for the effects of turbulence.

In order to compensate for the laser beam degradation, the effects of turbulence on the laser beam need to be characterized and understood. As a laser beam propagates through the atmosphere, it encounters turbulent eddies of air formed by the mixing of pockets of air of different temperature. The air pockets have different indices of refraction. The path the laser takes through the air is altered by variations in the index of refraction along its path. The cumulative result of these changes is a de-focusing of the laser beam. This de-focusing is similar to the effect seen when viewing an approaching car through heat rising from a hot road. The image of

1

the approaching car is altered or de-focussed as the light travels through pockets of different index of refraction generated by the heat radiating off the road.

Flow visualization techniques such as shadowgraphs, schlieren photography, and holographic interferometry have been used to view turbulent flows. These techniques are used for visualizing turbulent flows, but do not result in the information necessary to understand the effects of the turbulence on an optical wavefront.

Several researchers have published information on the effects of turbulence on optical wavefronts. Chew and Christiansen propagated a laser beam through a shear-layer flow and used far-field laser intensity profiles to investigate effects on the laser beam propagation [1]. They concluded that coherent structures in the shear-layer affect beam propagation and suggested that perturbing the shear layer would change the fluid mechanics of the flow and improve the time-averaged Strehl ratio. Jumper and Hugo examined turbulent flows using a small-apertured beam [4]. They measured the off-axis movements of a small diameter laser beam as it traversed a turbulent flow with varying indices of refraction. They found that they could quantify the beam jitter and use the measurements to calculate the optical path difference of the laser beam as it passed through the turbulent field. They concluded that the technique would provide spatial and temporal information about the expected effects of the turbulence on a much larger diameter laser beam.

Other researchers have used optical wavefront sensors which were designed to measure the distortion of planar wavefronts after passing through areas of varying index of refraction. Magee measured the effects of laboratory generated turbulence on an optical wavefront directly with a shearing interferometer [5]. By measuring the optical wavefront phase, he was able to calculate the phase structure function and average optical transfer function (OTF) of an incoherent imaging system in a manner that eliminated all assumptions about the structure of the turbulence.

For a more complete understanding of the index of refraction distribution within turbulent fields, three-dimensional images have been examined. Researchers

2

have shown that two-dimensional projections of three-dimensional objects can be combined by tomographic reconstruction techniques to produce three-dimensional images. Example projections of an object are shown in Figure 1. When two-dimensional projections of turbulent fields were taken with optical wavefront sensors, the resultant three-dimensional images represented the index of refraction distribution in the turbulent fields. Hesslink discussed several tomographic reconstruction techniques and a variety of flow visualization techniques that could be used to obtain the projections [2]. He pointed out that although there are several difficulties in acquiring simultaneous projections from a 180 degree arc around a flow field, the three-dimensional representations that result from tomographic reconstruction techniques can be obtained and provide much more information about a flow field than two-dimensional techniques. One of the primary measurement techniques he considered for acquiring his projections was holography recorded on film.
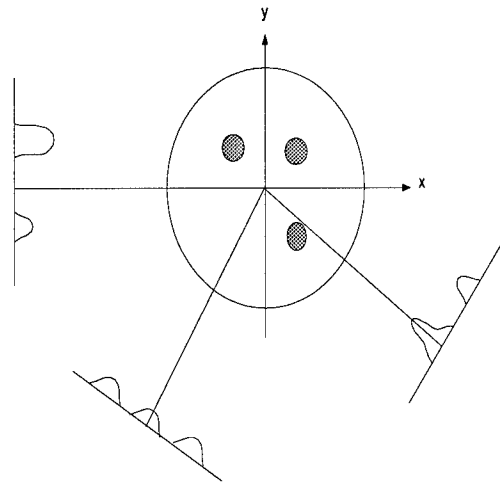
Figure 1.   Examples of projections of an object. The three dark circles produce different projections when viewed from different angles.

Johnson conducted a simulation that showed that tomographic reconstruction techniques could be combined with an optical wavefront sensor to reconstruct three-dimensional reconstructions of index of refraction distributions within turbulent flows [3]. He found that an accurate (less than 3% average error) three-dimensional re-

3

construction could be generated when as few as six projections were used. Pedersen verified that Johnson's simulation results could be obtained in a laboratory experiment [7]. He generated three-dimensional reproductions of the index of refraction distributions within a few jets of warm air using 16 projections from a shearing interferometer wavefront sensor.

1.2 Research Objectives

The scope of this effort was to use an SI optical wavefront sensor to visualize the effects of shear-layer turbulence on an optical wavefront. Shear-layers have been examined and visualized in many ways, but the effects of shear-layer turbulence on an optical wavefront have only been approximated. This research presents a way to visualize the optical wavefront distortion so that it may be understood. The shear-layer turbulence was viewed with the well-known shadowgraph flow visualization technique so that a comparison could be made between the structure of the flow as shown in the shadowgraph and the effects on the optical wavefront as measured with a shearing interferometer (SI) wavefront sensor.

1.3 Summary of Key Results

Phase maps showing the shape of distorted optical wavefronts after propagating through a shear-layer of nitrogen and helium are presented in this research. Results are presented for two orthogonal views of a shear-layer. One view shows that there are very abrupt changes in the wavefront shape in the region of the shear. The other view shows several peaks and valleys in the optical wavefront. For both cases, the amount of wavefront distortion grew as the distance from the shear-layer turbulence generator increased.

The results show a similarity between the basic structure viewed in the shadowgraphs and the shapes of the distorted wavefronts. Shadowgraphs are included for all of the shear-layer flows presented in this thesis to allow for a comparison be-

tween the shadowgraphs and the SI outputs. The shadowgraphs provide the second derivative of the indices of refraction in the flow, while the interference patterns provide information about the wavefront shape and phase. The interference patterns viewed on each of the six cameras of the SI produced images of the turbulence that provided a great deal of information about the structure of the turbulence and the shape of the optical wavefront. They were generated by interfering two images of the same flow. In the interference patterns, changes in intensity indicated changes in wavefront slope. The interference patterns were produced with a single collimated laser beam, a few mirrors, a polarizing beam splitter, and a camera. They could be used by themselves as a useful flow visualization technique.

1.4 Organization

Chapter II explains the theory behind optical wavefronts and optical wavefront sensors. Chapter III explains the design of the turbulence chamber and the experimental setup and procedures used to generate the shear-layer turbulence and then characterize the turbulence. Chapter IV presents the results of this research. Concluding remarks and recommendations for further study are given in Chapter V.

II. Background

When an optical wavefront propagates through a field of varying index of refraction, the wavefront is distorted. This chapter first defines optical wavefronts and explains how turbulence distorts them. It then discusses the Hartmann wavefront sensor and the shearing interferometer (SI) that have been used to measure phase perturbations caused by atmospheric turbulence.

2.1 Optical Wavefronts

The stars in the night sky provide a good example of distorted wavefronts. Stars appear to twinkle because of the distortion of planar wavefronts as they pass through pockets of turbulent air in the earth's atmosphere. Since stars are so far away, they are considered to be point sources. The wavefronts generated by stars are planar when they reach the top of the atmosphere. To reach the surface of the earth, the planar wavefronts pass through the atmosphere which is made up randomly sized moving pockets of air known as turbulent eddies. Eddies form when air masses of different temperatures mix and break apart into smaller and smaller eddies of different temperature [8]. Since the index of refraction of air is sensitive to temperature, each of the pockets has a slightly different index of refraction. As the planar wavefronts from the stars pass through randomly sized moving eddies of air, the wavefronts become distorted. Figure 2 shows an example of wavefront distortion due to turbulent eddies. This distortion varies with time and causes the twinkling of the stars.

Laser beams used for communications or weapon systems become distorted while passing through turbulence in the atmosphere. If the laser systems are mounted in airplanes or missiles, the laser beams experience further distortion while passing through the additional turbulence generated by the vehicle as it passes through the

6
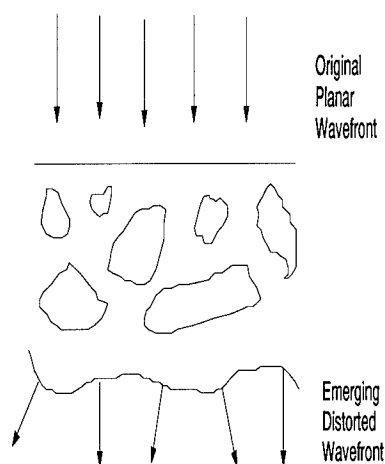
Figure 2. Wavefront distortion due to turbulent eddies.

air. The distortion degrades the performance of laser systems and can even cause mission failure.

2.2 Optical Wavefront Sensors

It is possible to measure the distortion of planar wavefronts using wavefront sensors. Wavefront sensors measure the slope of the phase along a wavefront. These measurements can be used to produce phase maps showing the shape of the wavefront after passing through a turbulent field. These measurements provide results that are proportional to a line integral through the index of refraction distribution along the direction of propagation of the wavefront but provide no information about the density or placement of the various indices of refraction located within the field. The two most common types of wavefront sensors are the Hartmann wavefront sensor and the Shearing Interferometer (SI).

The Hartmann wavefront sensor consists of an array of lenslets. Each lenslet focuses a segment of the wavefront onto an array of detectors. If the wavefront has no slope, each lenslet focuses its portion of the wavefront onto a spot at the center of its detector array. If the wavefront is tilted, the lenslets focus onto spots off center.
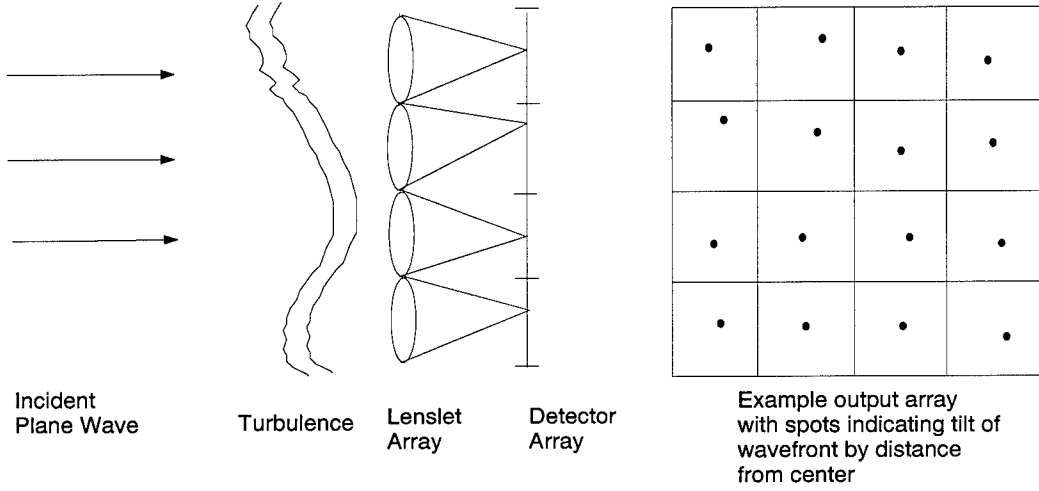
Figure 3. Diagram showing operation of a Hartmann wavefront sensor.

Figure 3 shows how a Hartmann wavefront sensor works. The position where the spot is focused is related to the slope by:

$$\theta(x,y) = \tan^{-1}\left(\frac{(x_c^2 + y_c^2)^{\frac{1}{2}}}{f_l}\right),\tag{1}$$

where $\theta(x,y)$ is the slope angle, x_c and y_c indicate the spot centroid location, and f_l is the lens focal length. The slope measurements from each of the lenses is combined to obtain a phase map of the wavefront.

The other commonly used wavefront sensor, the SI, uses a less direct method of measuring phase distortions in a wavefront. The SI measures the slope of a wavefront by interfering the wavefront with a spatially displaced (sheared) version of itself. The interference pattern produced is proportional to the slope of the wavefront in the direction of shear. By measuring the slope in two orthogonal shear directions, the wavefront can be fully characterized [5]. A diagram of the SI used in this research is shown in Figure 4.

The two legs of the SI operate the same way, but have orthogonal polarizations. One leg measures the slope in the x-direction and the other leg measures the slope

8
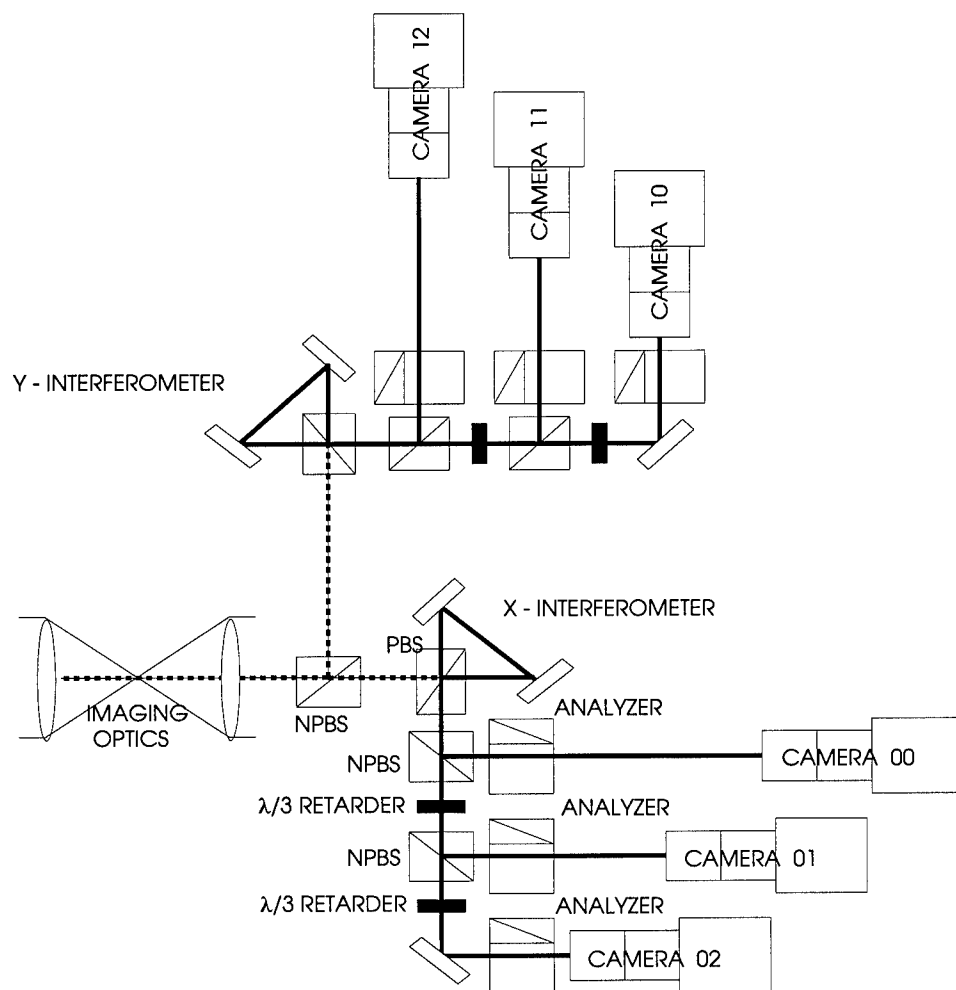
Figure 4. Diagram of a Shearing Interferometer.

X-direction
Shear Distance

Y-direction
Shear Distance
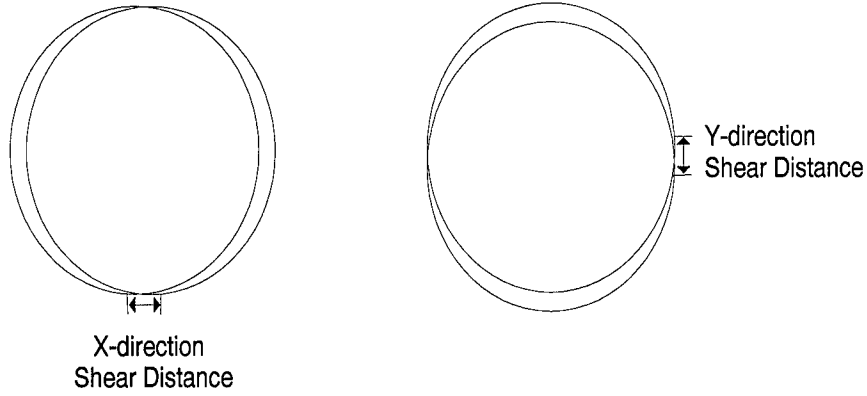
Figure 5. Lateral shear for the x and y directions.

in the y-direction. When the two sets of measurements are combined, a phase map showing the overall slope of the wavefront can be calculated. Figure 5 shows how the wavefront is displaced in the x and y directions, and Figure 6 shows the optical components used to produce a lateral shear.

Since the mathematics associated with the x-direction and y-direction lateral shear are basically the same, only the x-direction will be presented in this section. Let the complex amplitude, $\Phi(x, y)$, of the wavefront entering the SI be described by:

$$\Phi(x, y) = A(x, y) \exp^{j\phi(x,y)}, \tag{2}$$

where $A(x, y)$ is the amplitude, $\phi(x, y)$ is the path integrated phase, and x and y are transverse spatial coordinates. $\phi(x, y)$ is related to the index of refraction, $n(x, y, z)$, by:

$$\phi(x, y) = k \int_0^L n(x, y, z) ds, \tag{3}$$

where k is a constant, L is the distance through the turbulence, and ds is the incremental length along the propagation path.

A spatially shifted version of the optical field is described by:

$$\Phi(x + \Delta x, y) = A(x + \Delta x, y) \exp^{j\phi(x+\Delta x,y)}, \tag{4}$$

10
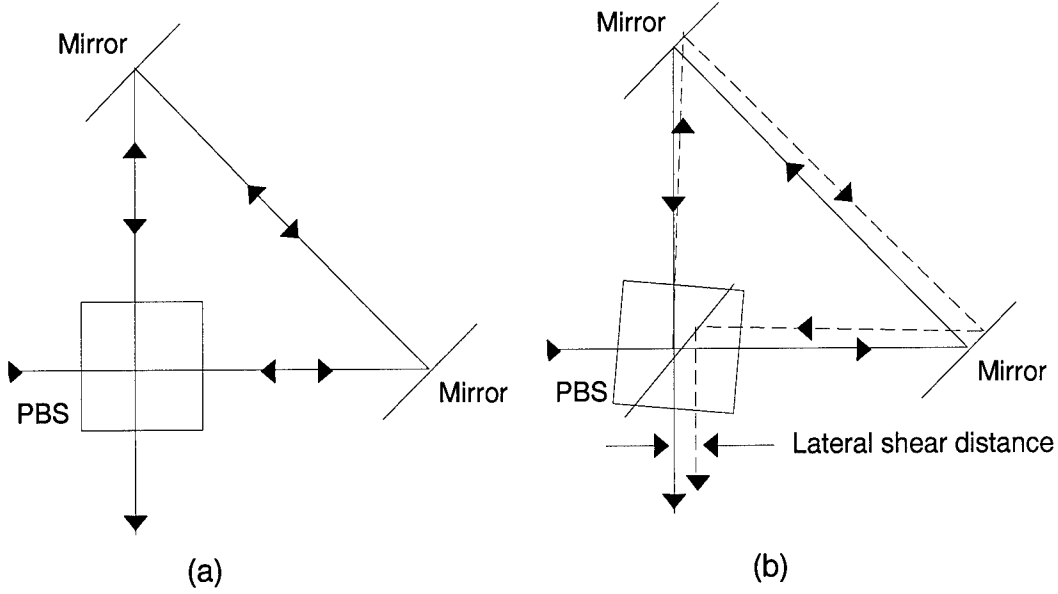
Figure 6. Optical components used to produce lateral shear. (a) No lateral shear. (b) Lateral shear produced by rotating the PBS.

where Δx is the shear distance in the x-direction. The interference pattern formed by combining the fields described in Equations (2) and (4) is described by the squared magnitude of the sum of the amplitudes:

$$|\Phi(x,y) + \Phi(x + \Delta x, y)|^2 = 2A^2[1 + cos(\Delta\phi)], \tag{5}$$

where

$$\Delta\phi = \phi(x,y) - \phi(x + \Delta x, y) \tag{6}$$

and $A(x,y)$ is assumed constant with respect to x. The intensity captured by each camera of the SI, apart from the scaling factor, is of the form:

$$I = 1 + \cos(\Delta\phi). \tag{7}$$

Figure 4 shows three cameras on each leg of the SI. The first camera on each leg captures the sheared interference pattern described by equation 7 and the second

and third cameras capture:

$$I_2 = 1 + \cos(\Delta\phi + \frac{\pi}{3}) \tag{8}$$

and

$$I_3 = 1 + \cos(\Delta\phi + \frac{2\pi}{3}). \tag{9}$$

The SI determines the phase difference, $\Delta\phi(x,y)$, of the wavefront by analyzing the interference patterns given in Equations (7), (8), and (9) [5]. The SI software combined the two orthogonal sets (x and y-directions) of interferograms collected by the SI and used least squares reconstruction [14] and three-bin reconstruction [9] algorithms to produce phase maps showing the optical wavefront phase.

2.3 Shadowgraphs

A shadowgraph is generated by transmitting light through a turbulent flow and recording the intensity pattern produced. The light is refracted and bent as it passes through the turbulence in response to changes in index of refraction. A particular light ray that would arrive at point (x_i, y_i) in the image plane without any turbulence present would get deflected to a point (x^*, y^*) with turbulence present. The resulting intensity, I^*, at point (x^*, y^*) results from all intensities that are deflected to the new point. The resulting intensity, $I^*(x^*, y^*)$ with turbulence present is given by [6]

$$I^*(x^*, y^*) = \sum_i \frac{I_i(x_i, y_i)}{\mid \partial(x^*, y^*)/\partial(x, y) \mid}. \tag{10}$$

Assume a single point, (x, y), is mapped into (x^*, y^*) and that the new coordinates are

$$x^* = x + \Delta x(x, y), y^* = y + \Delta y(x, y), \tag{11}$$

12

where Δx and Δy describe the displacement [6]

$$\Delta x = l \int_L \frac{1}{n} \frac{\partial n}{\partial x} dz, \tag{12}$$

and

$$\Delta y = l \int_L \frac{1}{n} \frac{\partial n}{\partial y} dz. \tag{13}$$

l is the distance from the recording plane to the exit plane of the test flow, n is the index of refraction, L is the width of the turbulence. A linearization of the mapping function is found by assuming that Δx and Δy are small and that products and higher powers of Δx and Δy can be neglected. The Jacobian is then

$$\mid \frac{\partial(x^*, y^*)}{\partial(x, y)} \mid \cong 1 + \frac{\partial \Delta x}{\partial x} + \frac{\partial \Delta y}{\partial y}. \tag{14}$$

With the above linearization, the relative changes in light intensity in the image plane are given by

$$\frac{(I^* - I)}{I} = \frac{\Delta I}{I} = l \int_L (\frac{\partial^2}{\partial x^2} + \frac{\partial^2}{\partial x^2})(\ln n) dz. \tag{15}$$

The index of refraction, n, of a gas is related to the gas density, ρ, and the Gladstone-Dale constant, K, by [6]:

$$n - 1 = K\rho. \tag{16}$$

The Gladstone-Dale constant depends on certain characteristics of the gas as well as the frequency or wavelength of the light used. A few examples of Gladstone-Dale constants are shown in Table 1 [6]. By applying the Gladstone-Dale formula, Equation 16, it becomes evident that the shadowgraph responds to the second derivative of flow density. Figure 7 shows a simple shadowgraph optical set-up.

Shadowgraphs give different results than the SI interference patterns. The SI interference patterns show phase information about the optical wavefront. The

13

Table 1. Gladstone-Dale Constants for Different Gases

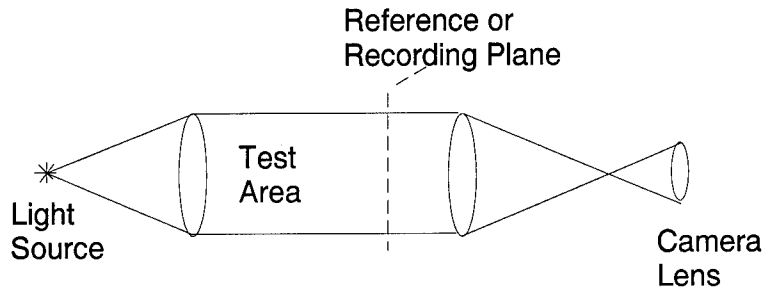| Gas	K (cm^3/g)	Wavelength (μm)	Temperature (K)
Air	0.2259	0.6074	288
Nitrogen	0.238	0.589	273
Helium	0.196	0.633	295

Figure 7. Optical components for producing a shadowgraph with parallel light through the test field.

interference patterns described by Equations (7), (8), and (9) are related to the index of refraction of the flows by the integral shown in Equation (3). The shadowgraphs respond to the second derivative of flow density which is related to the index of refraction as shown in Equation (16).

III. Experimental Setup and Procedures

A turbulence chamber was designed and constructed for the purpose of applying optical wavefront sensor flow visualization techniques to an actual flow field with a complicated three-dimensional structure. The turbulence chamber was designed to allow two gases with different indices of refraction to be brought together at different velocities forming a turbulent mixing layer. The shear-layer turbulence generated by this type of chamber has been studied by many different researchers using several flow visualization techniques [1, 11, 12, 15]. The wavefront phase of a collimated helium-neon laser beam was measured by an SI after passing through the turbulence. The phase differences, or slope measurements, were then reconstructed to form a phase map showing the structure of the phase.

Figure 8 shows a block diagram of the experiment. Plane-waves were propagated through the shear-layer turbulence. The perturbed wavefronts were sensed by the optical wavefront sensor and converted into two-dimensional arrays containing the slope of the wavefronts. The wavefront slope estimates were then converted to wavefront phase and displayed in the phase maps. The phase maps represent the shape of the optical wavefront.

In this chapter, a description is given of the equipment, optical setup, and procedures used to generate the phase maps. Section 3.1 presents some information about the shearing interferometer. Section 3.2 describes the shear-layer turbulence generator and the method used to measure the output gas velocities. Section 3.3 discusses the optical setup. Section 3.4 explains the experimental procedures used to calibrate the SI and acquire and analyze the data.

3.1 Shearing Interferometer

The shearing interferometer and associated software located in the AFIT Adaptive and Atmospheric Optics Laboratory was used to measure the optical wavefronts

Planar Optical Wavefront — Turbulence — Optical Wavefront Sensor (Shearing Interferometer) — Measurement of Distorted Optical Wavefront — Phase Map
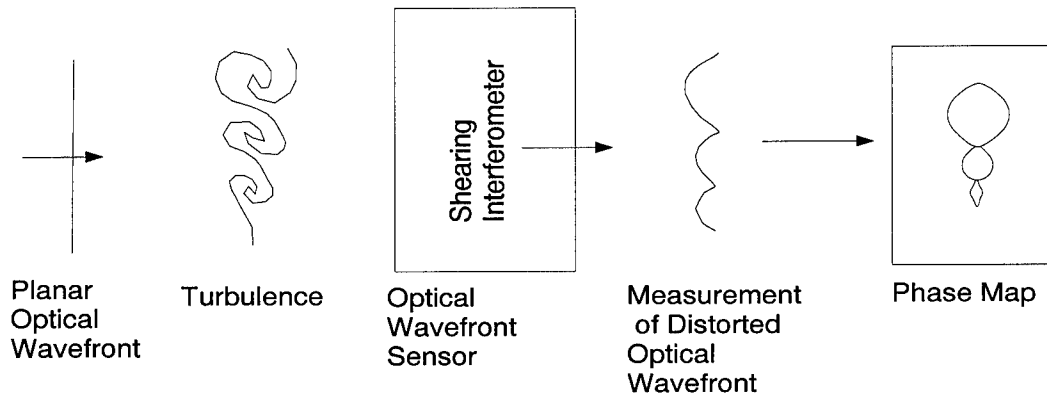
Figure 8. Block diagram of the experimental setup.

during the experiment. The spatial resolution of the sensor at the measurement aperture was approximately 0.5 millimeters. The SI has a sensitivity of 0.0237 waves and could sense phase changes as large as 0.1 waves per pixel [5]. A 75 milliwatt helium-neon laser at a wavelength of 632.8 nm was collimated, propagated through the turbulence, and measured by the SI. Figure 4 shows the Shearing interferometer used for this experiment.

Each of the six SI cameras captured interference patterns that are described in the background section of this thesis. These interference patterns were viewed real-time during the experiment on television monitors. The images showed the structure of the shear-layer flow. Figures 36, 37, and 38 show the relationships of Equations 7, 8, and 9. Figures 39, 40, and 41 show the same relationship, but in an orthogonal direction. The effect of changing gas velocities was viewed real-time.

The gas velocities used in this thesis were picked by viewing the interference patterns on the television monitors and selecting the velocities that showed the most structure within the aperture. Once the flow was established by setting the gas velocities, a set of frames were captured.

Figures 42 and 43 show computer generated interferograms. The interference patterns were produced by digitally computing the interference pattern resulting

16

from interfering the calculated wavefront with plane waves having a tilt of 10 waves in the either the x-direction or the y-direction. The interferograms generated during this research for the shear-layer were included as another means of visualizing the turbulence. They are analogous to holograms and contain fringes that are separated by distances proportional to the slope of the wavefront in the x or y directions. For a more detailed description of the shearing interferometer, including the mathematics describing its operation, the reader is referred to Magee [5].

Once the six interference patterns were captured, the SI generated two sum images containing the scaled sum of the three x-direction images and three y-direction images. The SI used the scaled sums to calculate the x and y direction tilt for each point within the aperture. The wavefront slope estimates were then combined in a linear fashion and converted to wavefront phase. Examples of phase maps are shown in Figures 44, 45, and 46.

3.2 Shear-layer Turbulence Generator

The small low-speed wind-tunnel contained two chambers separated by a splitter plate. The tunnel allowed two streams of gas to mix at a sharp trailing edge and form a shear-layer. A side view of the shear-layer turbulence generator is shown in Figure 9, and a top view of the shear-layer turbulence generator is shown in Figure 10.

The outer dimensions of the box were 14 cm x 14 cm x 43 cm. It was constructed out of 2,54 cm thick aluminum. All seams were sealed with rubber tubing so that the box would not leak any gas. Each gas entered a 9 x 4.5 cm stilling chamber through 0.635 cm plastic tubing and exited through a 2.5 x 1.25 cm opening creating a 13:1 contraction ratio. The chamber size was reduced following a third order polynomial. Referencing the center of the box as (0,0) and starting at a point 10 cm from the output end of the box, the polynomial on each curve goes from 4.5
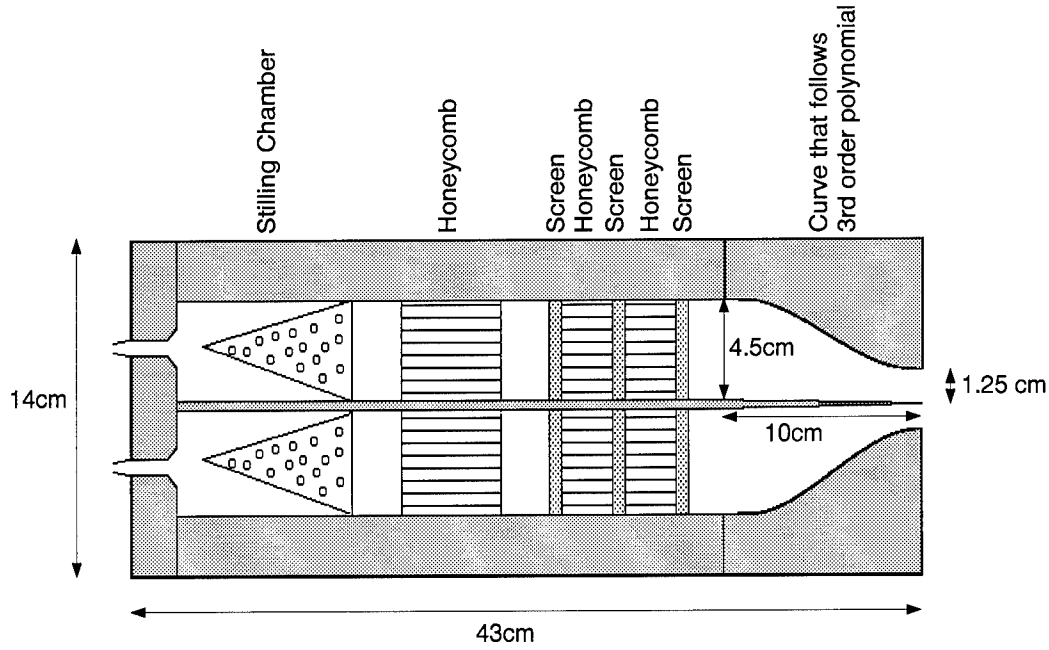
Figure 9. Side view of the shear-layer turbulence generator.

cm to 1.25 cm following the equation:

$$y = 0.0080x^3 - 0.1120x^2 - 0.0005x + 4.4695. \tag{17}$$

A pyramid filled with 0.5 cm holes was placed in each chamber to distribute the flow of gas evenly across each chamber. Honeycomb and screens were placed in the tunnels to straighten the flow and reduce the free-stream turbulence. The splitter plate was made out of 0.32cm thick bronze plate and was tapered over 10 cm to a sharp edge. The inside of one of the chambers can be seen in Figure 11 and the front of the turbulence generator can be seen in Figure 12.

To view the structure of the shear-layer turbulence, the gases had to have different indices of refraction from each other and the room temperature air. Where the gases mixed together, the change in index of refraction was measured by the SI. Areas in the flow that experienced a gradient in the index of refraction were displayed by the SI as areas with changing slope. Areas of constant index of refraction appeared
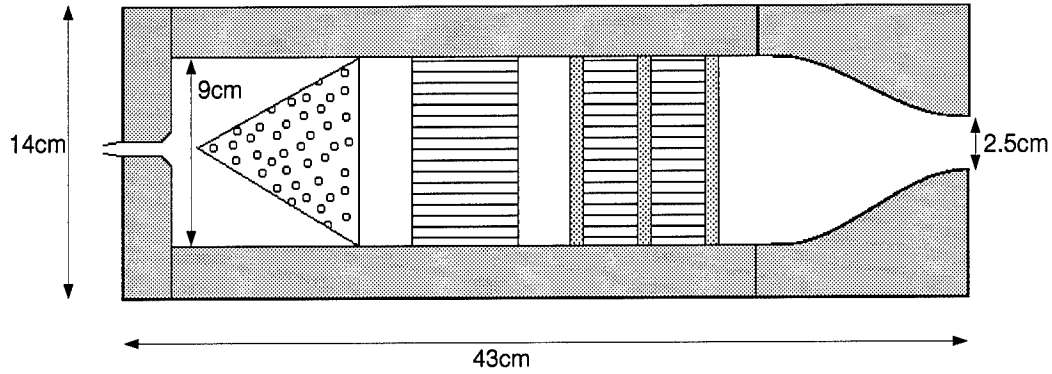
18

Figure 10. Top view of the shear-layer turbulence generator.

Table 2. Indices of Refraction of gases at 1 atm and 0° C

Gas	Index of Refraction
Air	1.000294
Nitrogen	1.00030
Helium	1.000036

flat. The two gases used were Helium and Nitrogen. The indexes of refraction of the gases are listed in Table 2.

3.2.1 Velocity measurements.   Prior to acquiring data, the gas velocities were measured. The velocities, v, were calculated using a form of Bernoulli's equation:

$$v = \sqrt{\frac{2\Delta P}{\rho}}, \tag{18}$$

where ΔP is the difference between the pressure measured leaving the chamber and atmospheric pressure, and ρ is the gas density [10]. ΔP was measured directly and ρ was calculated with the following formula:

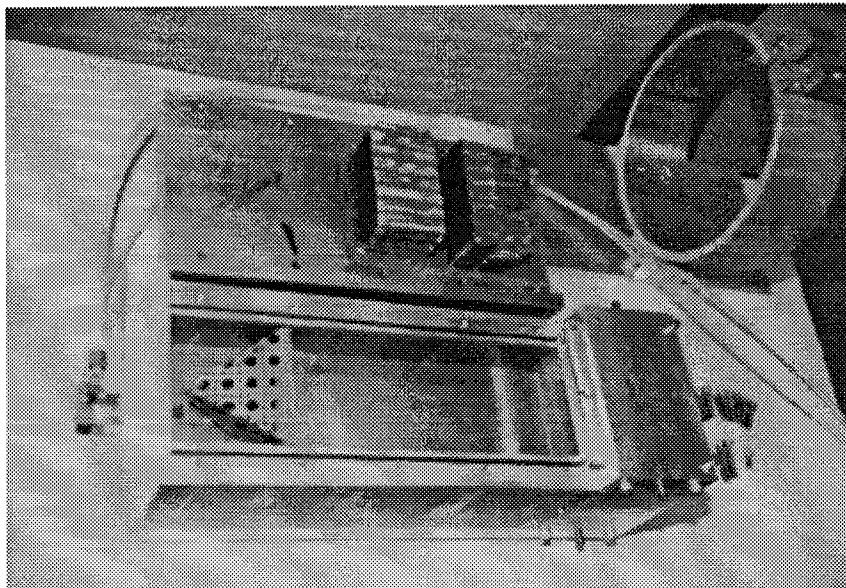$$\rho = \frac{p}{RT}, \tag{19}$$

19

Figure 11.   Top view of the turbulence generator showing the pyramid, honeycomb, and screens that fit inside one of the chambers.
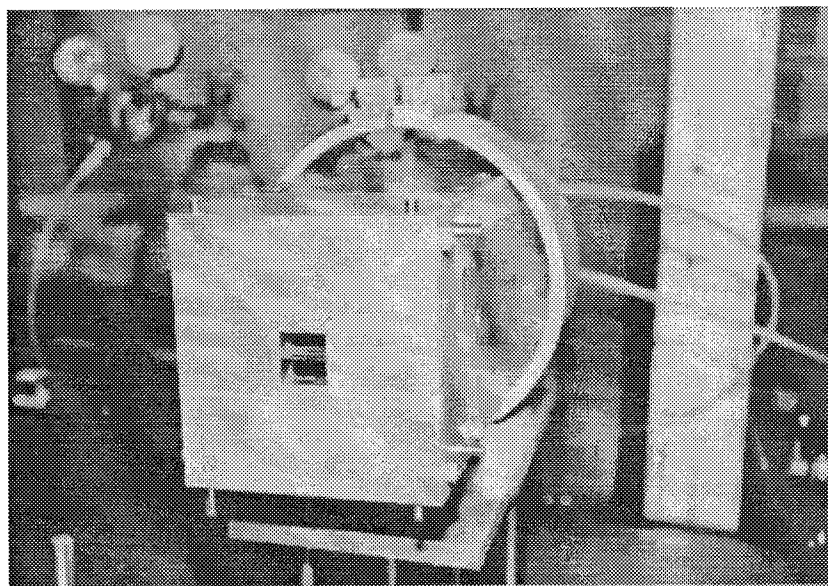

Figure 12.   Front view of the shear-layer turbulence generator. The splitter plate can be seen in the center of the 2.5 cm x 2.5 cm opening.

Table 3. Engineering Gas Constants

Gas	Engineering Gas Constant R (N m/kg K)
Air	286.8
Nitrogen	296.5
Helium	2076.8

where p is the pressure of the gas, R is the engineering gas constant, and T is the gas temperature. The gas constants are listed in Table 3 [13].

A micro manometer was used to measure ΔP in inches of water. It was accurate up to 0.001 ± 0.0005 inches of water (0.00254 ± 0.00127 cm of water). This error in ΔP translates into a velocity uncertainty of ± 0.09 m/sec for helium and ± 0.07 m/sec for nitrogen in the velocity range reported in this research.

The regulator for each gas was adjusted to provide the desired velocity. This allowed the gas flows to be turned on and off several times during each data gathering session. The velocities were also measured after the data was collected to make sure the velocities remained constant. Throughout the experiment, the averages of the velocities were 8.3 ± 0.3 m/sec for the helium and 1.5 ± 0.2 m/sec for the nitrogen.

3.3 Optical Setup

The experimental setup used by Magee [5] and Pedersen [7] was expanded for use in the current experiment. Figure 13 shows the optics used on the optical bench to visualize the turbulence.

The 75mw helium-neon laser beam was collimated and passed through a one inch polarizing beam splitter (PBS). The vertically polarized one inch square beam passed through the turbulence. A plane in front of the shear-layer turbulence generator was then imaged through lens 1 to a point at aperture 1. The aperture was set to a small opening to filter out noise. Lens 2 re-imaged the turbulence after passing
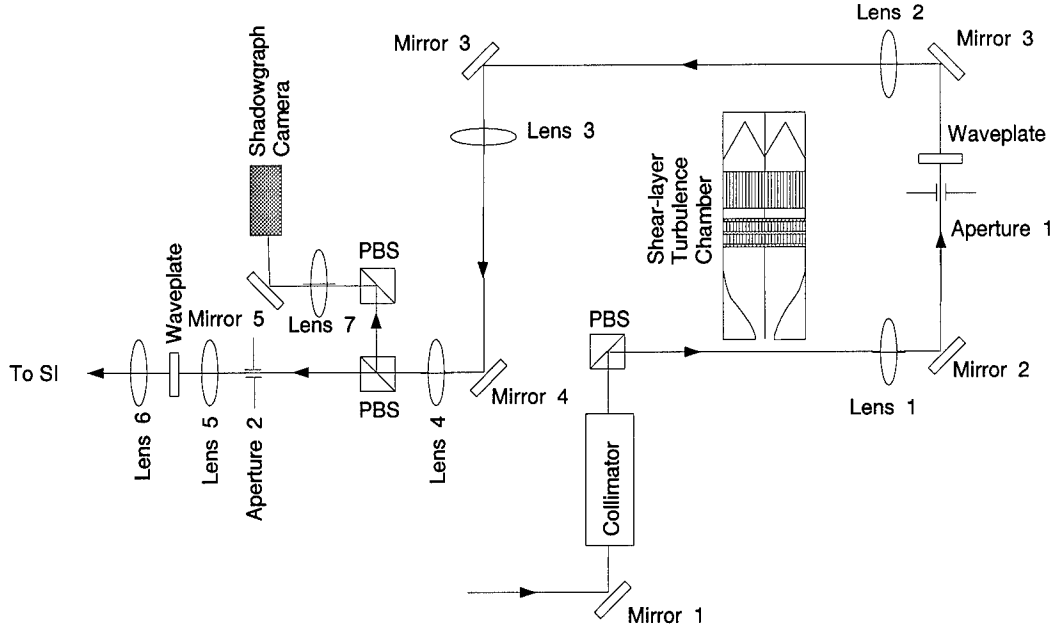
Figure 13. Diagram of the optical setup.

through a wave plate that rotated the polarization to horizontal. Lenses 3 and 4 re-imaged a demagnified image of the turbulence at aperture 2. Aperture 2 is the 1.8 cm diameter input aperture for the SI. The PBS after lens 4 passes only horizontally polarized light. Lenses 5 and 6 re-image the turbulence at the SI. The wave plate between lenses 5 and 6 was used to adjust the polarization of the laser beam during calibration of the SI. A camera was placed after lens 7 to capture a shadowgraph of the turbulence. The shadowgraph camera was placed within the focal length of lens 7 at the point where the field of view of the shadowgraph camera was the same as the field of view of the SI cameras.

3.4   Experimental Procedures

The general procedure followed to gather the data using the SI was very similar to that followed by Magee [5] and Pedersen [7]. Details for each procedure are explained in [5]. A general description will be presented here with the reason for

22

each procedure. This section begins with a description of the SI calibration and ends with a description of the data acquisition and analysis.

3.4.1 Calibration.   After an initial 30 minute warm-up of the laser, the camera gains were calibrated to each other by measuring laser intensities through several optical filters. Any inconsistencies between the camera measurements were compensated for by adding or subtracting an offset for each pixel value on each camera. This adjustment was accomplished so the cameras would all measure the same intensities for each pixel. This calibration was important since the intensity of each pixel carries the data needed to produce the phase map. Next, the cameras were aligned to each other so they would all image the same wavefront. Finally, the shift and shear measured by each of the cameras were calibrated. Small points of laser light produced by placing a pinhole in the aperture plane of the SI were viewed on each of the cameras for single polarizations. The centroid of the spots were measured for each camera. By doing this measurement at both horizontal and vertical polarizations, the lateral shear distance shown in Figures 5 and 6 were measured. An average of several shift and shear measurements was used to calibrate the SI.

3.4.2 Data acquisition and analysis.   Once the SI was calibrated and the gas velocities measured, data was collected. Sets of reference data were collected prior to and after each shear-layer data set. The reference data measured the distortion of the system with no turbulence present in the optical path. In theory, the reference wavefront should be planar, but imperfections in the optics and slight misalignments of the optical components caused the reference wavefront to be non-planar. During analysis, the reference wavefronts were subtracted from the wavefronts acquired with the shear-layer turbulence in the laser path. The resulting wavefront represented the phase perturbation caused by the shear-layer turbulence only. The stability of the

reference wavefronts was checked by taking several reference frames during the data acquisition.

Several sections of the shear-layer turbulence were viewed during each data gathering session. Since the aperture used on the SI was an 1.8 cm circle, the shear-layer chamber was moved 1.8cm between each data set. Data was gathered at 0.0 to 1.8 cm, 1.8 - 3.6 cm, and 3.6 - 5.4 cm locations. The measurements were taken from the front of the shear-layer turbulence generator to the laser beam edge as shown in Figure 13.

IV. Results

In this chapter, the results of the experiment are presented. The first section presents the results of viewing the shear-layer turbulence from the side as shown in Figure 14. This view showed the nitrogen on the top, the helium on the bottom, and the region where the gases mixed in the center. These images will be referred to as the side view images in this thesis. The next section presents the results of the orthogonal view of the shear-layer turbulence as shown in Figure 15. These images will be referred to as the top view images.

For each data set, shadowgraphs, images from some of the SI cameras, interferograms for the x and y directions, and phase maps are presented. The turbulence was viewed at three different locations through a 1.8 cm circular aperture. It was viewed at 0.0 - 1.8 cm, 1.8 - 3.6 cm, and 3.6 - 5.4 cm downstream from the output of the shear-layer turbulence generator as shown if Figures 14 and 15. All images represent views where the gas flows were moving from right to left. Figures 16 - 20 and Figures 27 - 31 show three images. The left image in each figure represents the same instant in time, the center images all represent another instant in time, and the right images all represent a third instant in time. Each figure illustrates a different method of viewing the same turbulence. The three images in each figure are presented together to show how the turbulence increased as the distance from the turbulence generator increased. They do not represent a continuous gas flow, but do represent the same gases at the same velocities at different times.

4.1 Data showing side view of shear-layer turbulence

The shadowgraphs in Figure 16 show the vortices that are commonly seen in side view images of shear-layer turbulence. The lines follow the mixing region where the two gases mix. They were generated as a simple way to view the turbulence. The intensity changes in the shadowgraphs are related to the second derivative of
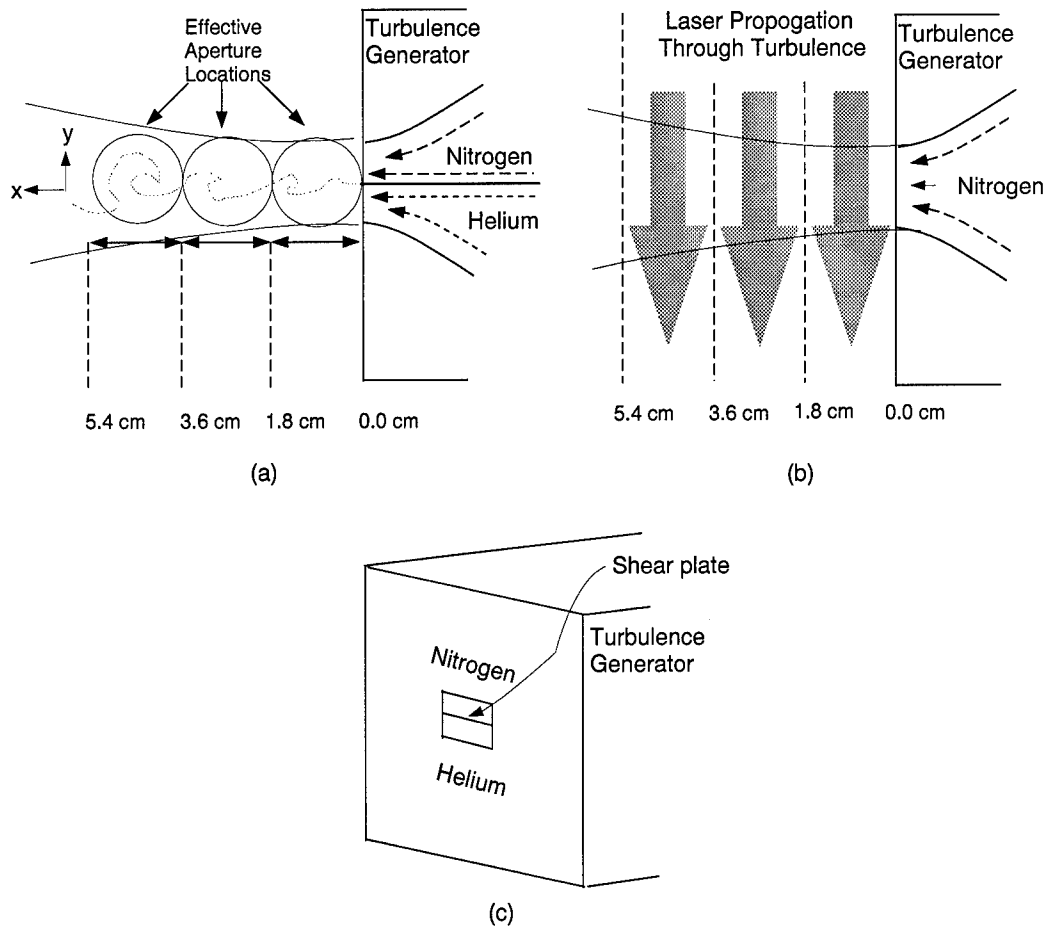
Figure 14. (a) The orientation of the turbulence chamber and effective aperture locations for side view images. The nitrogen flows from the top, the helium flows from the bottom, and the mixing region is in the center. (b) Laser propagation through the shear-layer for the 0.0 - 1.8 cm, 1.8 - 3.6 cm, and 3.6 - 5.4 cm locations as measured from the front of the turbulence generator. (c) Orientation of the turbulence generator for side view images.
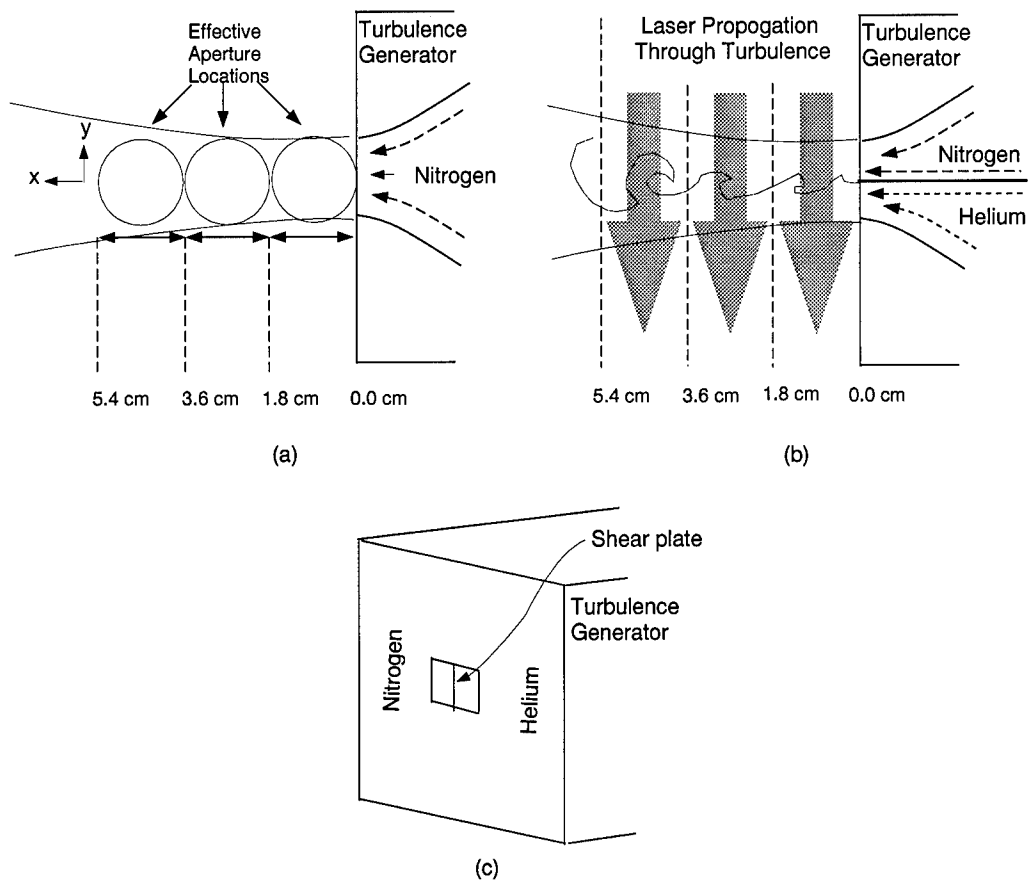
26

Figure 15. (a) The orientation of the turbulence chamber and effective aperture locations for top view images. The laser propagates through the nitrogen and helium in a direction that is orthogonal to the mixing layer of the gases. (b) Laser propagation through the shear-layer for the 0.0 - 1.8 cm, 1.8 - 3.6 cm, and 3.6 - 5.4 cm locations as measured from the front of the turbulence generator. (c) Orientation of the turbulence generator for top view images.

27

the index of refraction. There are also diffraction effects seen in the shadowgraphs due to using a monochromatic laser source to illuminate the turbulence rather than white light. Diffraction lines are present for the lines showing the mixing layer and around the edges of the images. The shadowgraphs allow for a comparison of a well known flow visualization technique to the outputs of the SI wavefront sensor.

The interference patterns in Figure 17 show the basic structure contained in the shadowgraphs in Figure 16. The lines in the shadowgraphs fall in the same locations as some of the lines in the interference patterns. The interference patterns have wide regions of changes in intensity rather than just lines like the shadowgraphs. These changes in intensity indicate changes in wavefront slope in the vertical direction (y-direction shown in Figure 14) of the images. The interference patterns represent the wavefront shape and has intensities variations that are related to the wavefront phase by Equation (7). Therefore, the interference patterns provide information about the turbulence like the shadowgraphs, but the interference patterns provide additional information about the optical wavefront shape. The images in Figure 18 provide information about the wavefront slope in the horizontal direction (x-direction shown in Figure 14). They do not resemble the shadowgraphs as well as the y-direction interference patterns, but do show that there are changes in wavefront slope in the horizontal direction. This indicates that the majority of the structure viewed in the shadowgraph is due to gradients in the index of refraction in the y-direction.

The images shown in Figures 19 and 20 are similar to holograms. They were generated by digitally interfering a tilted plane wave with a data set containing the wavefront slope information. The fringe separation in Figure 19 is proportional to the wavefront slope in the x-direction and the fringe separation in Figure 20 is proportional to the wavefront slope in the y-direction. These images present the same information as the interference patterns in Figures 17 and 18 through fringe separation rather than changes in intensity.

Phase maps are shown in Figures 21 - 23. They were displayed in a manner that would allow their shape and the structure shown in the shadowgraphs and interference patterns to be compared. The curves shown in the phase maps follow the same curves shown in the shadowgraphs and interference patterns. The phase maps show the overall phase of the optical wavefront after passing through the shear-layer turbulence. The x-direction and y-direction slopes of the interference patterns were linearly combined for each pixel and converted to phase maps showing the overall phase of the optical wavefront. There are areas of zeros within the phase maps where the gases combine. This can be explained as regions where the slope is too steep for the resolution of the SI. The SI is only capable of measuring a slope change of 0.1 waves per pixel. If the slope exceeds this amount, the pixel is assigned a value of zero. Another possible explanation for some of the zeros is that the light was refracted so much in those regions that little or no light reached the cameras. The phase maps in Figures 24, 25, and 26 show side views of the same data so the amplitudes can be seen. The phase maps of the side view show that there are very abrupt changes in the wavefront shape in the region of the shear. For these results, the wavefront was distorted by as much as six waves (1 wave = 632.8 nm). The amount of distortion also grew larger as the downstream distance of the measurement location from the shear-layer turbulence chamber increased. A planar wavefront with no distortion would have an amplitude of zero. The smooth slopes in the figures show that the gases on either side of the shear-layer affected the optical wavefront also. The smooth slopes on both sides of the mixing region could indicate that the gas densities decreased as the distance from the mixing region increased. With decreasing density, the overall index of refraction changes affecting the optical wavefront would also decrease.
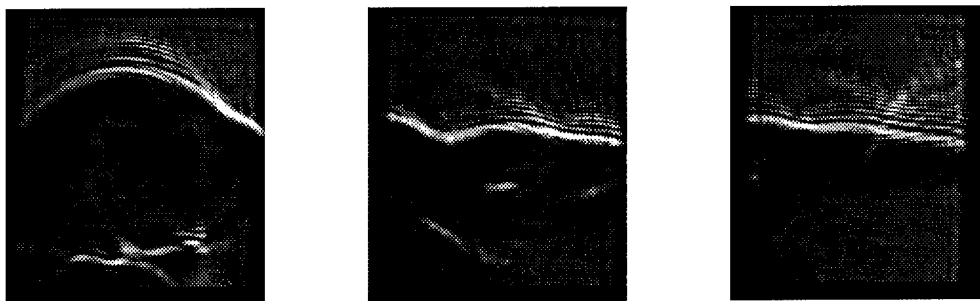
Figure 16.   Shadowgraphs for 5.4 cm - 3.6 cm, 3.6 cm - 1.8 cm, and 1.8 cm - 0.0 cm from the shear flow chamber (side view). Gas flow is from right to left. Helium velocity is 8.3 m/sec. Nitrogen velocity is 1.5 m/sec.
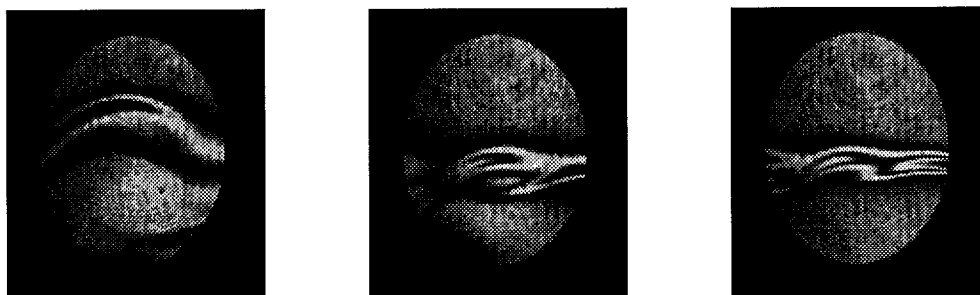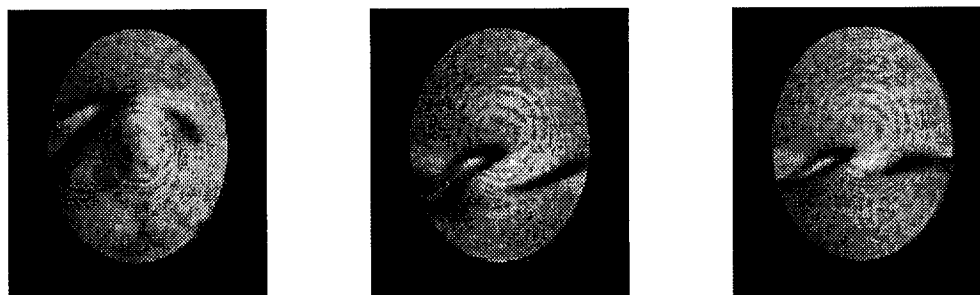

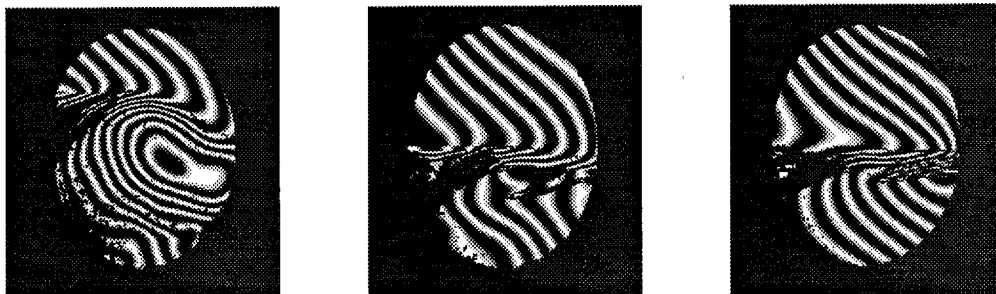Figure 17.   Camera 1,1 interference patterns for 5.4 cm - 3.6 cm, 3.6 cm - 1.8 cm, and 1.8 cm - 0.0 cm from the shear flow chamber (side view). Shear is in the y-direction. Gas flow is from right to left. Helium velocity is 8.3 m/sec. Nitrogen velocity is 1.5 m/sec.

Figure 18.   Camera 0,0 interference patterns for 5.4 cm - 3.6 cm, 3.6 cm - 1.8 cm, and 1.8 cm - 0.0 cm from the shear flow chamber (side view). Shear is in the x-direction. Gas flow is from right to left. Helium velocity is 8.3 m/sec. Nitrogen velocity is 1.5 m/sec.

Figure 19. x-direction interferogram patterns for 5.4 cm - 3.6 cm, 3.6 cm - 1.8 cm, and 1.8 cm - 0.0 cm from the shear flow chamber (side view). The fringe separation is proportional to the wavefront slope in the x direction. Gas flow is from right to left. Helium velocity is 8.3 m/sec. Nitrogen velocity is 1.5 m/sec.
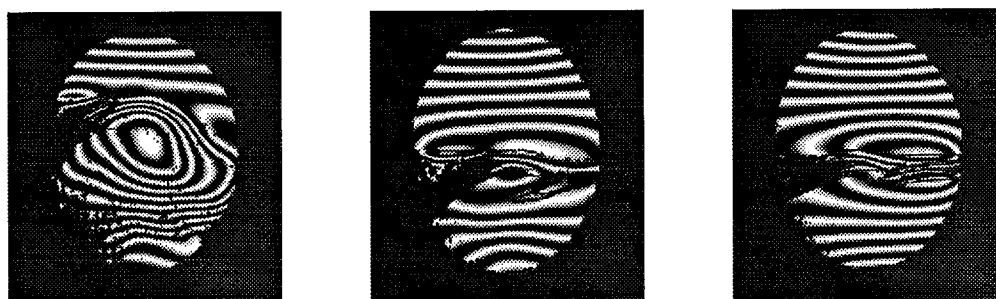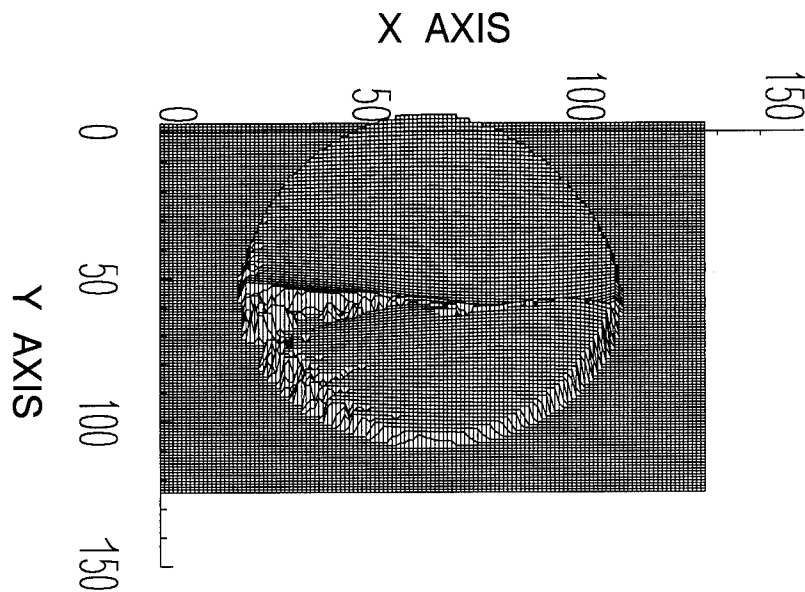

Figure 20. y-direction interferogram patterns for 5.4 cm - 3.6 cm, 3.6 cm - 1.8 cm, and 1.8 cm - 0.0 cm from the shear flow chamber (side view). The fringe separation is proportional to the wavefront slope in the y direction. Gas flow is from right to left. Helium velocity is 8.3 m/sec. Nitrogen velocity is 1.5 m/sec.

Figure 21. Phase map for 1.8 cm - 0.0 cm from the shear flow chamber (side view). Gas flow is from right to left. Helium velocity is 8.3 m/sec. Nitrogen velocity is 1.5 m/sec.
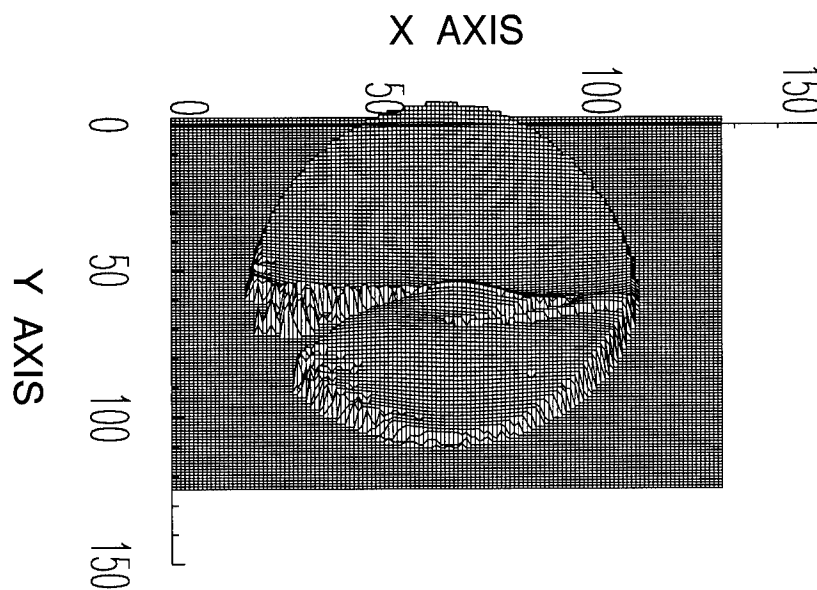
Figure 22. Phase map for 3.6 cm - 5.4 cm from the shear flow chamber (side view). Gas flow is from right to left. Helium velocity is 8.3 m/sec. Nitrogen velocity is 1.5 m/sec.
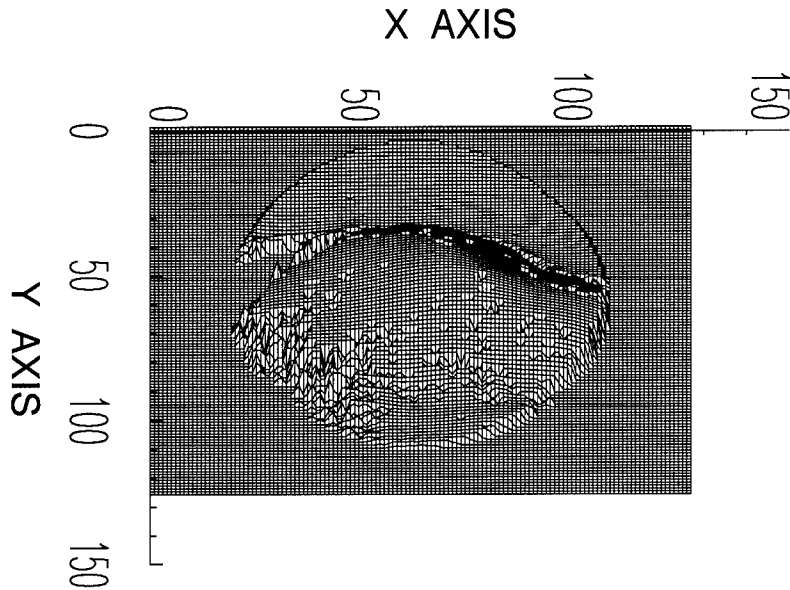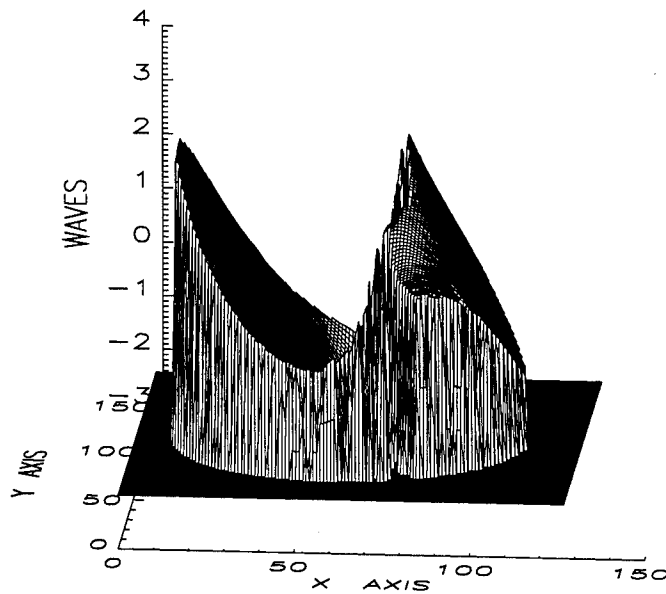
Figure 23. Phase map for 5.4 cm - 3.6 cm from the shear flow chamber (side view). Gas flow is from right to left. Helium velocity is 8.3 m/sec. Nitrogen velocity is 1.5 m/sec.

Figure 24. Phase map 2 for 1.8 cm - 0.0 cm from the shear flow chamber (side view). Gas flow is from right to left. Helium velocity is 8.3 m/sec. Nitrogen velocity is 1.5 m/sec. (The x and y axes in this figure correspond to the y and x-directions respectively)
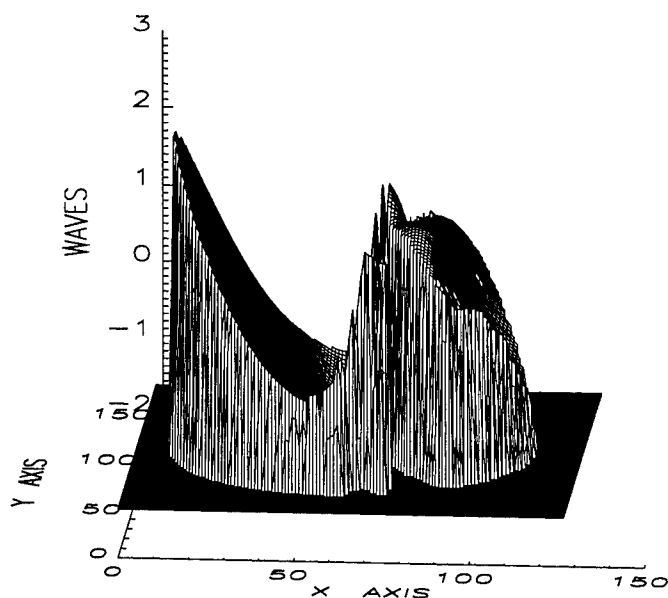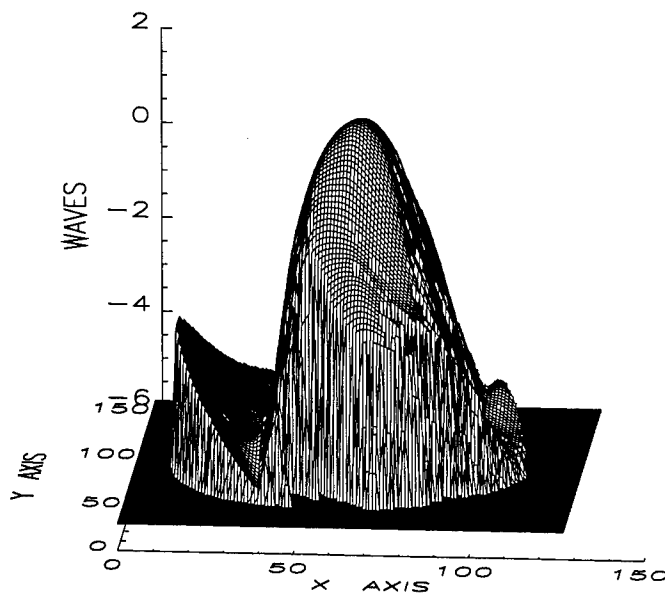
33

Figure 25.   Phase map 2 for 3.6 cm - 1.8 cm from the shear flow chamber (side view). Gas flow is from right to left. Helium velocity is 8.3 m/sec. Nitrogen velocity is 1.5 m/sec. (The x and y axes in this figure correspond to the *y* and *x*-directions respectively)

Figure 26.   Phase map 2 for 5.4 cm - 3.6 cm from the shear flow chamber (side view). Gas flow is from right to left. Helium velocity is 8.3 m/sec. Nitrogen velocity is 1.5 m/sec. (The x and y axes in this figure correspond to the *y* and *x*-directions respectively)

4.2 Data showing top view of shear-layer turbulence

The shadowgraphs in Figure 27 show the top view of shear-layer turbulence. They were generated so the structure viewed within the shear-layer could be compared to the outputs of the wavefront sensor.

The interference patterns shown in Figure 28 show the basic structure contained in the shadowgraphs shown in Figure 27. The lines in the shadowgraphs fall in the same locations as the changes in intensity in the interference patterns. The changes in intensity indicate changes in wavefront slope in the horizontal direction (x-direction) of the images. The intensities in the interference patterns are related to the wavefront phase by Equation (7). Figure 29 represents the wavefront slope in the y-direction. They are not as closely related to the shadowgraphs as the interference patterns shown in Figure 28, but show changes in the wavefront slopes in the x-direction. A complete set of images for all of the SI cameras is in the Appendix.

The fringe separation in Figure 30 is proportional to the wavefront slope in the x-direction and the fringe separation in Figure 31 is proportional to the wavefront slope in the y-direction. These images are digitally generated holograms of the wavefront. These images were generated by digitally interfering a tilted plane wave with a data set containing the wavefront slope information. They show the same information as the interference patterns in Figures 28 and 29 through fringe separation rather than changes in intensity.

The phase maps are shown in Figures 32 - 34. They show the same basic structure as the shadowgraphs and interference patterns. The peaks and valleys of the phase maps fall in the same locations as the intensity changes in the interference patterns. Slowly changing intensities correspond to slowly changing slope and major changes in intensity correspond to steep slopes. The amplitudes of the phase maps indicate the height of the peaks and the depth of the valleys of wavefront distortion grew as the distance from the shear-layer generator increased. The wavefront was distorted by as much as two waves (1 wave = 632.8 nm).
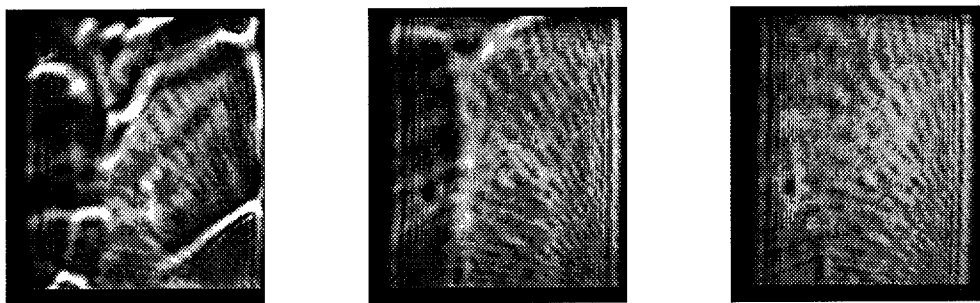
Figure 27.   Shadowgraphs for 5.4 cm - 3.6 cm, 3.6 cm - 1.8 cm, and 1.8 cm - 0.0 cm from the shear flow chamber (top view). Gas flow is from right to left. Helium velocity is 8.3 m/sec. Nitrogen velocity is 1.5 m/sec.
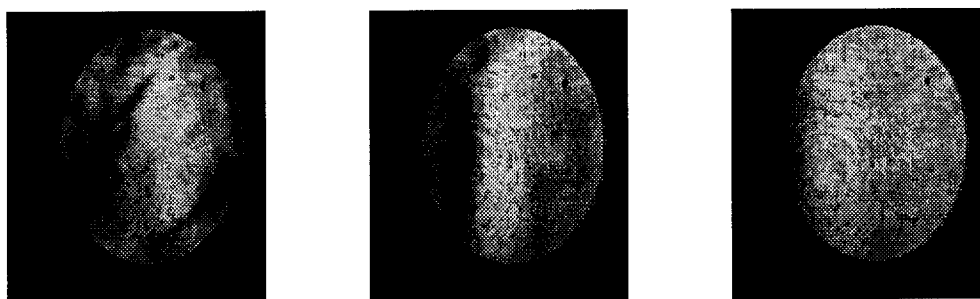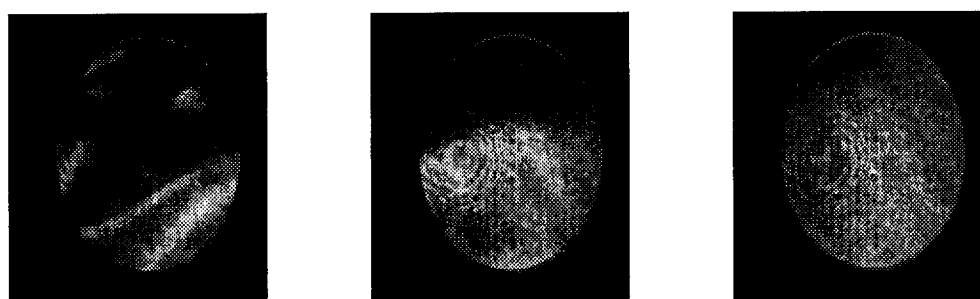

Figure 28.   Camera 0,2 interference patterns for 5.4 cm - 3.6 cm, 3.6 cm - 1.8 cm, and 1.8 cm - 0.0 cm from the shear flow chamber (top view). Shear is in the x-direction. Gas flow is from right to left. Helium velocity is 8.3 m/sec. Nitrogen velocity is 1.5 m/sec.

Figure 29.   Camera 1,0 interference patterns for 5.4 cm - 3.6 cm, 3.6 cm - 1.8 cm, and 1.8 cm - 0.0 cm from the shear flow chamber (top view). Shear is in the y-direction. Gas flow is from right to left. Helium velocity is 8.3 m/sec. Nitrogen velocity is 1.5 m/sec.

Figure 30. *x*-direction interferogram patterns for 5.4 cm - 3.6 cm, 3.6 cm - 1.8 cm, and 1.8 cm - 0.0 cm from the shear flow chamber (top view). The fringe separation is proportional to the wavefront slope in the x direction. Gas flow is from right to left. Helium velocity is 8.3 m/sec. Nitrogen velocity is 1.5 m/sec.
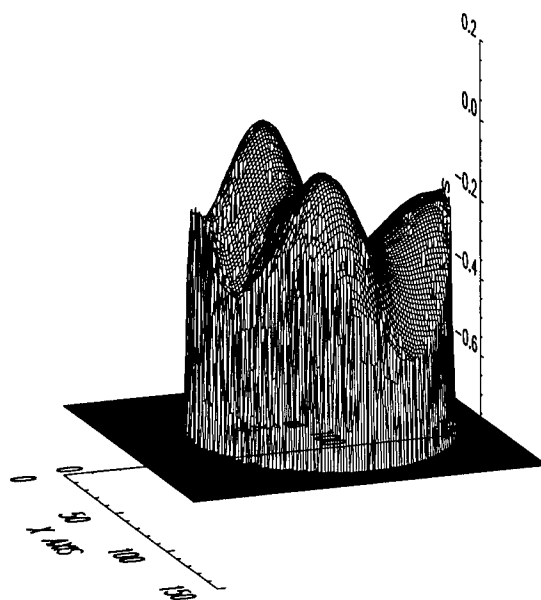

Figure 31. *y*-direction interferogram patterns for 5.4 cm - 3.6 cm, 3.6 cm - 1.8 cm, and 1.8 cm - 0.0 cm from the shear flow chamber (top view). The fringe separation is proportional to the wavefront slope in the y direction. Gas flow is from right to left. Helium velocity is 8.3 m/sec. Nitrogen velocity is 1.5 m/sec.

37

Figure 32. Phase map for 1.8 cm - 0.0 cm from the shear flow chamber (top view). Gas flow is from right to left. Helium velocity is 8.3 m/sec. Nitrogen velocity is 1.5 m/sec. (The x axis in this figure corresponds to the y-direction)
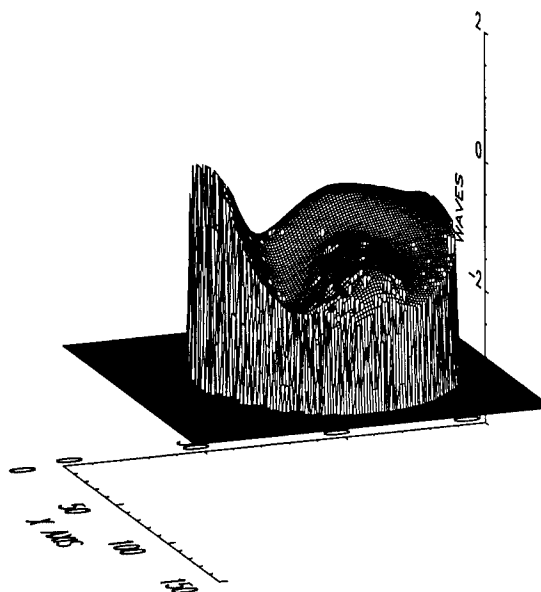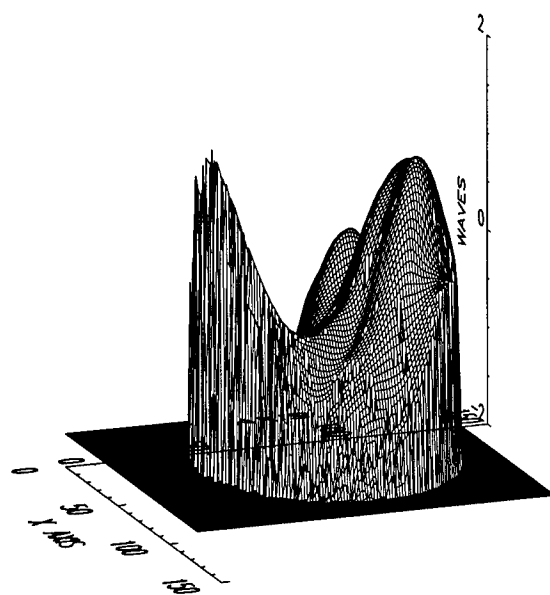

Figure 33. Phase map for 3.6 cm - 1.8 cm from the shear flow chamber (top view). Gas flow is from right to left. Helium velocity is 8.3 m/sec. Nitrogen velocity is 1.5 m/sec. (The x axis in this figure corresponds to the y-direction)

Figure 34.   Phase map for 5.4 cm - 3.6 cm from the shear flow chamber (top view). Gas flow is from right to left. Helium velocity is 8.3 m/sec. Nitrogen velocity is 1.5 m/sec. (The x axis in this figure corresponds to the *y*-direction)

V. Conclusions

The experiment showed that the distortion a planar optical wavefront experiences when passing through a shear-layer flow can be visualized and quantized. A shear-layer was viewed from the side and top by a shearing interferometer (SI) optical wavefront sensor. Shadowgraphs of the turbulence allowed a comparison to be made between the outputs of the SI and a well known flow visualization technique. Interference patterns from each of the six SI cameras showed wavefront slope information. Interferograms, similar to holograms, contained fringes with separation proportional to the wavefront slope in the x and y directions. Phase maps provided a way to view and quantize the shape of the optical wavefronts after passing through the turbulence. The turbulence was visualized at 0.0 - 1.8 cm, 1.8 - 3.6 cm, and 3.6 - 5.4 cm regions as measured from the shear-layer turbulence generator.

A shear-layer turbulence generator was designed and built that produced repeatable shear-layer flows. The basic structure of the flow could be repeated by maintaining the gas velocities. The helium velocity was maintained at 8.3 ± 0.3 m/sec and the nitrogen velocity was maintained at 1.5 ± 0.2 m/sec. The shadowgraphs showed the vortices that are commonly seen in shear-layer turbulence by other flow visualization techniques. A comparison was made between the structure seen in the shadowgraphs and the images produced by the SI wavefront sensor. It was also found that lines in the shadowgraphs were oriented in the same location as either peaks or valleys in the distorted wavefront.

The interference patterns viewed by each camera of the SI provided much more information about the turbulence than the shadowgraphs. The intensity variations in the interference patterns followed the general shapes shown in the shadowgraphs, but also indicated changes in wavefront slope. The interference patterns are related directly to wavefront phase. The shadowgraphs are only related to the index of refraction in the flow by a second derivative. The interference patterns required only

40

a few more optical components than the shadowgraph, and provided more information about the turbulence. With a single laser beam, two mirrors, and a polarizing beam splitter, the interference patterns showed a pattern that was proportional to the wavefront phase. It should be noted that the interference patterns only represent the wavefront slope in a single direction, but that was enough to provide much insight into the effects of the turbulence on the optical wavefront.

The SI also provided interferograms that are similar to holograms. They were produced by digitally interfering a tilted planar wavefront with the distorted wavefront. These interferograms provided slope information in two orthogonal directions. The fringe separation is proportional to wavefront slope. The interferograms didn't provide any new information, but did provide a different way to view the wavefront slope. They may also be useful to readers who are used to working with holograms.

By combining two orthogonal sets of interference patterns, the SI produced phase maps showing the phase of the optical wavefronts after passing through the shear-layer turbulence. The curves shown in the phase maps follow the curves shown in the shadowgraphs and interference patterns. The phase maps also allowed the amount of distortion of the wavefronts to be quantized. For the side view, the wavefront was distorted by as much as six waves (1 wave = 632.8 nm). For the top view, the wavefront was distorted by as much as two waves. The amount of distortion grew larger in both cases as the distance from the shear-layer turbulence chamber increased. There were also peaks and valleys in both cases. For the side view, there was a steep slope along the mixing area of the two gases. The slope gradually changed as the distance from the mixing layer region increased. For the top view, the peaks and valleys grew as the propagated away from the shear-layer turbulence generator. This indicated that the amount of distortion at a given location would oscillated between a peak and a valley.

Follow on work could be done with the shear-layer chamber used in this research. One possible area of research could include the use of different gases. The

helium and nitrogen had such different indexes of refraction that the SI could not reproduce the steep slopes between the gases. Possibly, nitrogen and compressed or heated air would produce better results.

Another area of possible research could involve faster cameras. The cameras on the SI were too slow to capture any temporal changes in the turbulence. From frame to frame, the flow appeared to jump around rather than progress forward or propagate away from the shear-layer turbulence generator. Another use for faster cameras could be to simultaneously capture the flow from different angles. This approach would allow tomographic reconstruction algorithms to be used to produce three-dimensional reconstructions of the turbulence. Several Hartmann wavefront sensors would be more practical to use than the SI for this approach, but the Hartmann wavefront sensors would not produce the interference patterns that appeared so interesting in this research.

Appendix A. Complete data set for side view of shear-layer turbulence
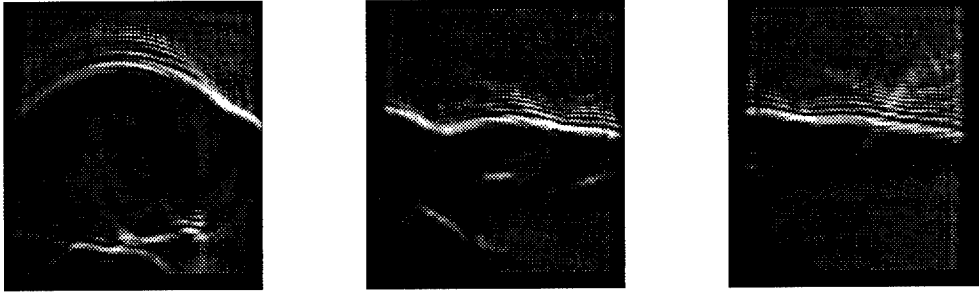
Figure 35.   Shadowgraphs for 5.4 cm - 3.6 cm, 3.6 cm - 1.8 cm, and 1.8 cm - 0.0 cm from the shear flow chamber (side view). Gas flow is from right to left. Helium velocity is 8.3 m/sec. Nitrogen velocity is 1.5 m/sec.
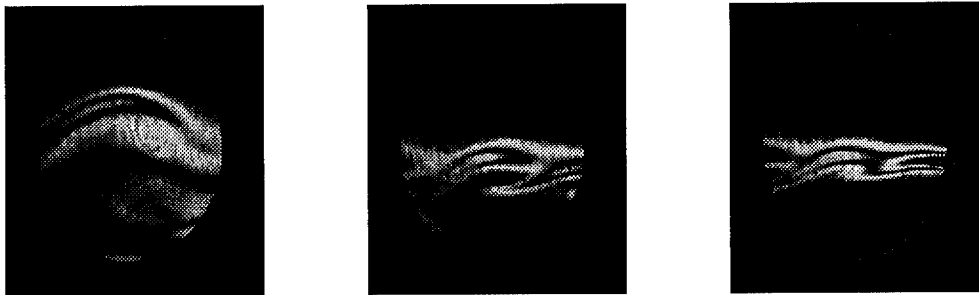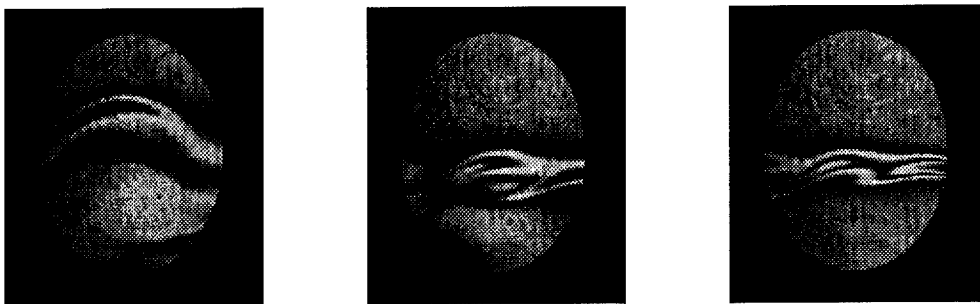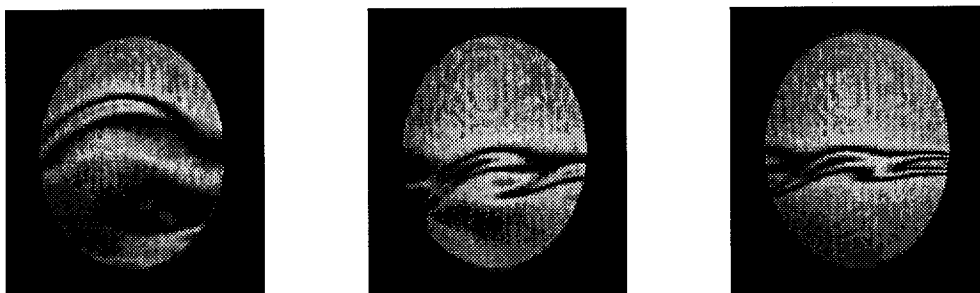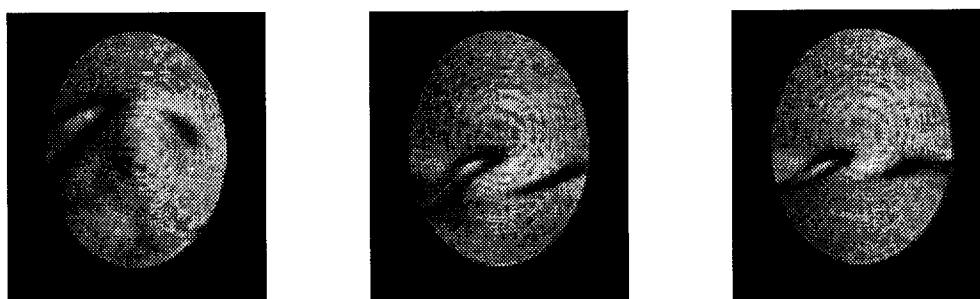

Figure 36.   Camera 1,0 interference patterns for 5.4 cm - 3.6 cm, 3.6 cm - 1.8 cm, and 1.8 cm - 0.0 cm from the shear flow chamber (side view). Shear is in the y-direction. Gas flow is from right to left. Helium velocity is 8.3 m/sec. Nitrogen velocity is 1.5 m/sec.
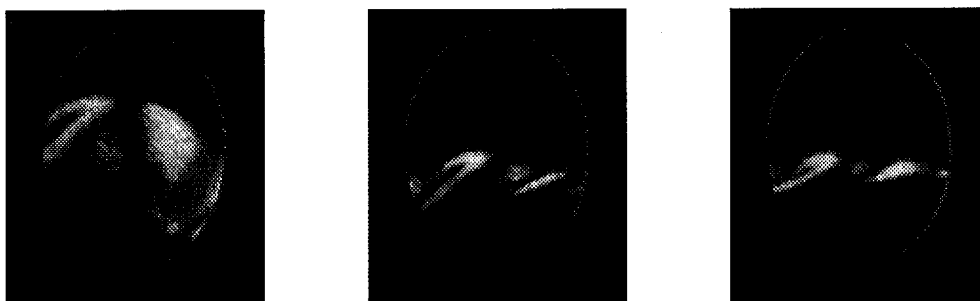
43

Figure 37.   Camera 1,1 interference patterns for 5.4 cm - 3.6 cm, 3.6 cm - 1.8 cm, and 1.8 cm - 0.0 cm from the shear flow chamber (side view). Shear is in the y-direction. Gas flow is from right to left. Helium velocity is 8.3 m/sec. Nitrogen velocity is 1.5 m/sec.

Figure 38.   Camera 1,2 interference patterns for 5.4 cm - 3.6 cm, 3.6 cm - 1.8 cm, and 1.8 cm - 0.0 cm from the shear flow chamber (side view). Shear is in the y-direction. Gas flow is from right to left. Helium velocity is 8.3 m/sec. Nitrogen velocity is 1.5 m/sec.
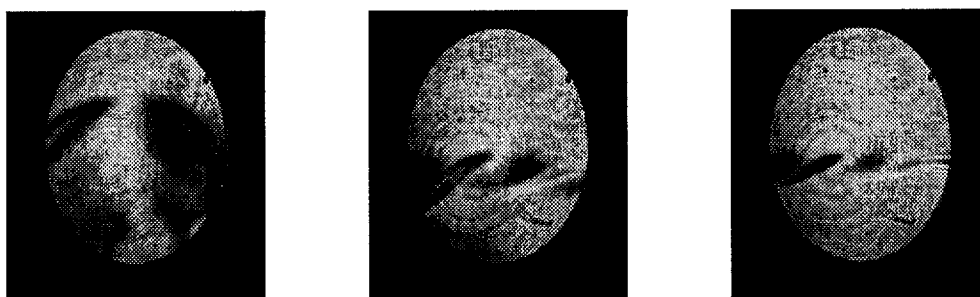

Figure 39.   Camera 0,0 interference patterns for 5.4 cm - 3.6 cm, 3.6 cm - 1.8 cm, and 1.8 cm - 0.0 cm from the shear flow chamber (side view). Shear is in the x-direction. Gas flow is from right to left. Helium velocity is 8.3 m/sec. Nitrogen velocity is 1.5 m/sec.

44

Figure 40. Camera 0,1 interference patterns for 5.4 cm - 3.6 cm, 3.6 cm - 1.8 cm, and 1.8 cm - 0.0 cm from the shear flow chamber (side view). Shear is in the x-direction. Gas flow is from right to left. Helium velocity is 8.3 m/sec. Nitrogen velocity is 1.5 m/sec.
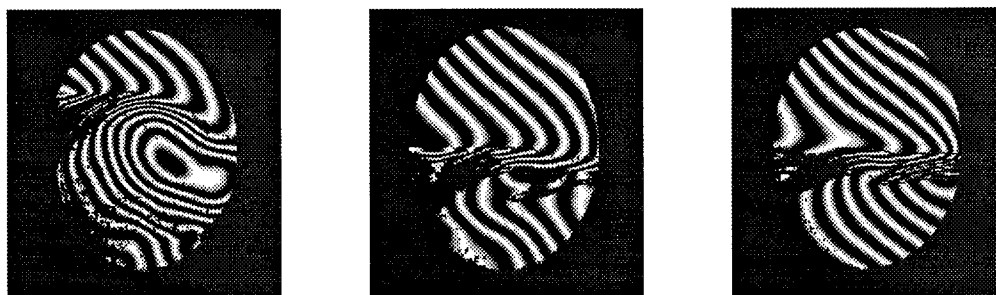

Figure 41. Camera 0,2 interference patterns for 5.4 cm - 3.6 cm, 3.6 cm - 1.8 cm, and 1.8 cm - 0.0 cm from the shear flow chamber (side view). Shear is in the x-direction. Gas flow is from right to left. Helium velocity is 8.3 m/sec. Nitrogen velocity is 1.5 m/sec.

Figure 42. x-direction interferogram patterns for 5.4 cm - 3.6 cm, 3.6 cm - 1.8 cm, and 1.8 cm - 0.0 cm from the shear flow chamber (side view). The fringe separation is proportional to the wavefront slope in the x direction. Gas flow is from right to left. Helium velocity is 8.3 m/sec. Nitrogen velocity is 1.5 m/sec.
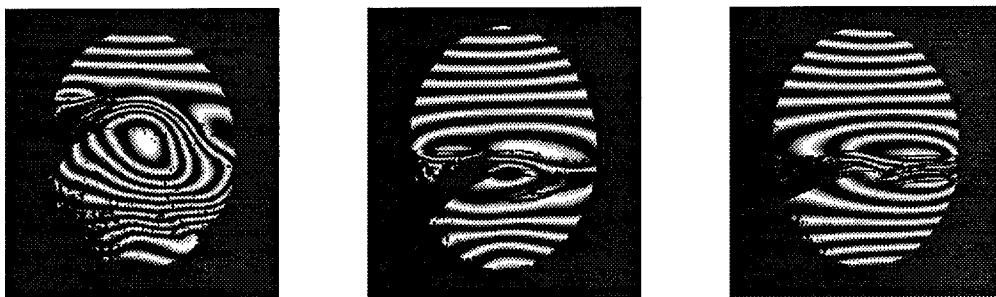
Figure 43. y-direction interferogram patterns for 5.4 cm - 3.6 cm, 3.6 cm - 1.8 cm, and 1.8 cm - 0.0 cm from the shear flow chamber (side view). The fringe separation is proportional to the wavefront slope in the y direction. Gas flow is from right to left. Helium velocity is 8.3 m/sec. Nitrogen velocity is 1.5 m/sec.
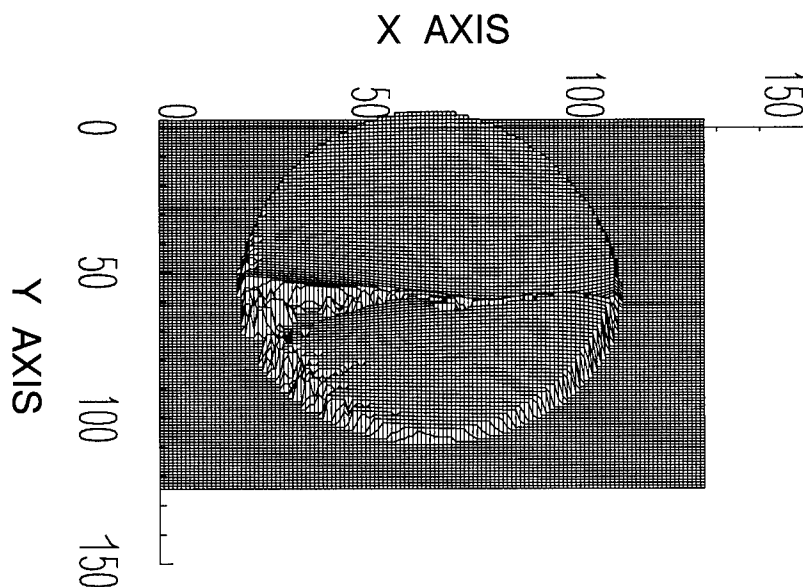

Figure 44. Phase map for 1.8 cm - 0.0 cm from the shear flow chamber (side view). Gas flow is from right to left. Helium velocity is 8.3 m/sec. Nitrogen velocity is 1.5 m/sec.
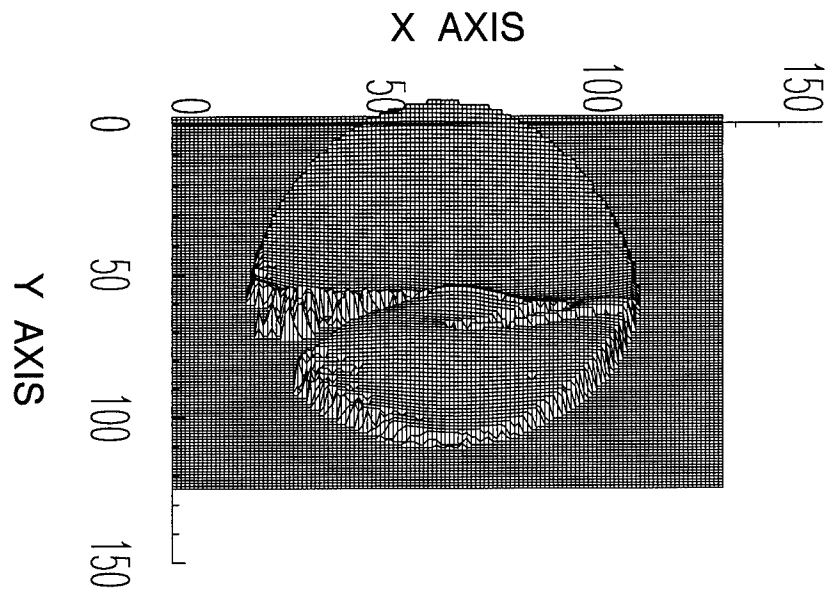
Figure 45. Phase map for 3.6 cm - 1.8 cm from the shear flow chamber (side view).
Gas flow is from right to left. Helium velocity is 8.3 m/sec. Nitrogen
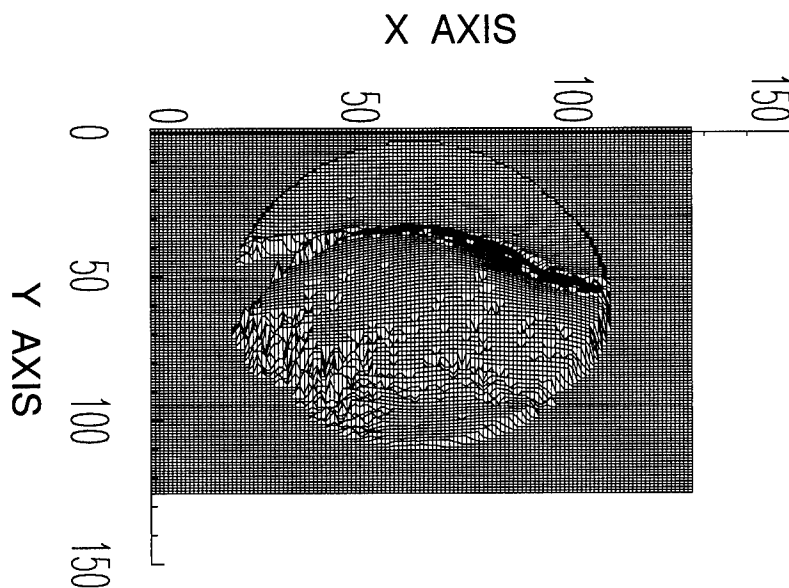velocity is 1.5 m/sec.

Figure 46. Phase map for 5.4 cm - 3.6 cm from the shear flow chamber (side view).
Gas flow is from right to left. Helium velocity is 8.3 m/sec. Nitrogen
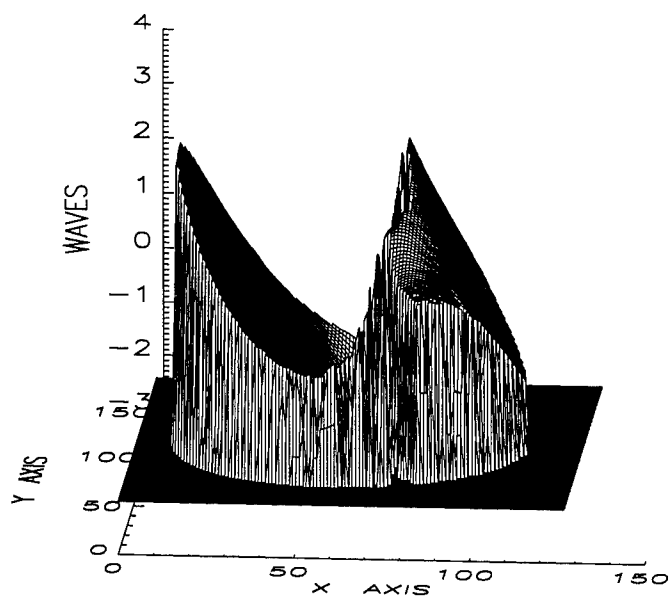velocity is 1.5 m/sec.

Figure 47. Phase map 2 for 1.8 cm - 0.0 cm from the shear flow chamber (side view). Gas flow is from right to left. Helium velocity is 8.3 m/sec. Nitrogen velocity is 1.5 m/sec. (The x and y axes in this figure correspond to the y and x-directions respectively)
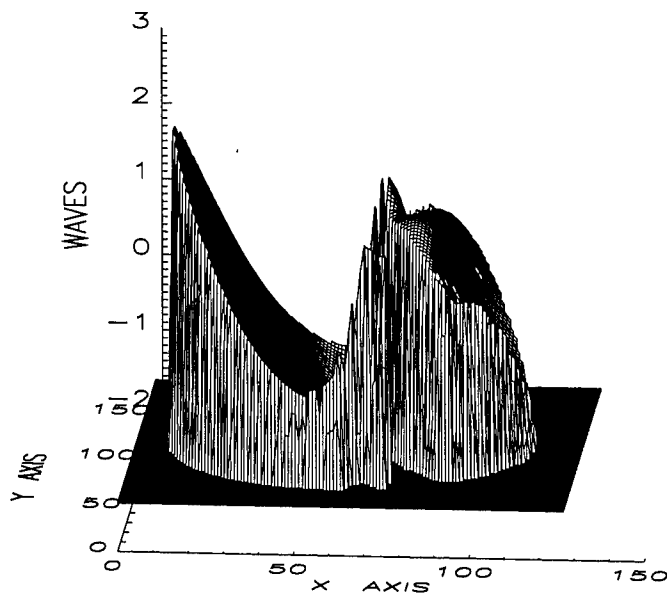

Figure 48. Phase map 2 for 3.6 cm - 1.8 cm from the shear flow chamber (side view). Gas flow is from right to left. Helium velocity is 8.3 m/sec. Nitrogen velocity is 1.5 m/sec. (The x and y axes in this figure correspond to the y and x-directions respectively)
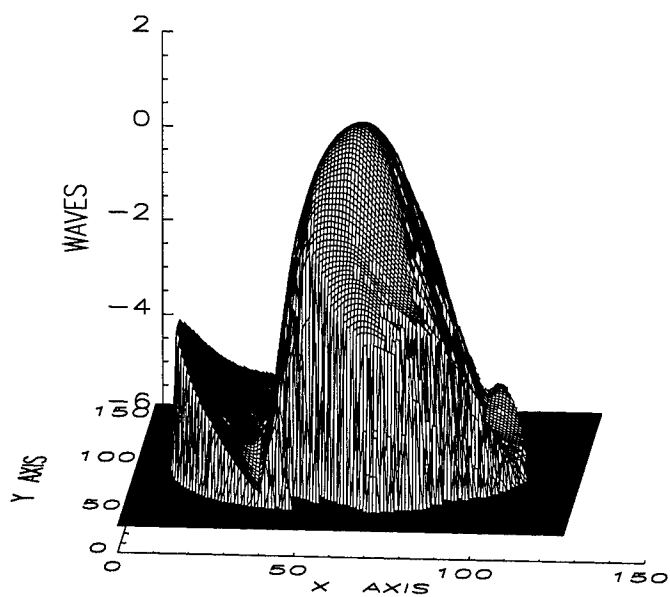
Figure 49.   Phase map 2 for 5.4 cm - 3.6 cm from the shear flow chamber (side view). Gas flow is from right to left. Helium velocity is 8.3 m/sec. Nitrogen velocity is 1.5 m/sec. (The x and y axes in this figure correspond to the y and x-directions respectively)

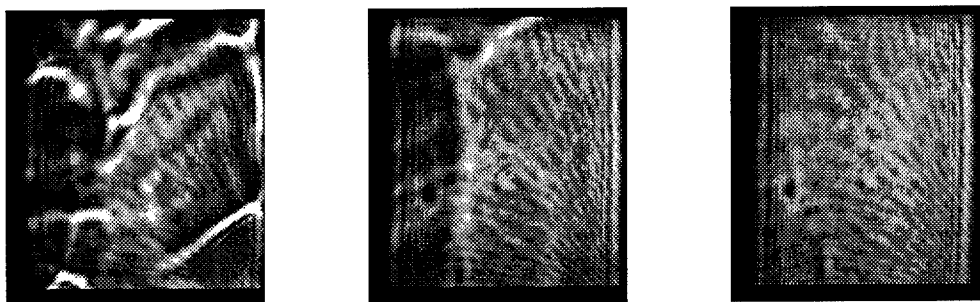*Appendix B. Complete data set for top view of shear-layer turbulence*

Figure 50. Shadowgraphs for 5.4 cm - 3.6 cm, 3.6 cm - 1.8 cm, and 1.8 cm - 0.0 cm
from the shear flow chamber (top view). Gas flow is from right to left.
Helium velocity is 8.3 m/sec. Nitrogen velocity is 1.5 m/sec.

Figure 51. Camera 1,0 interference patterns for 5.4 cm - 3.6 cm, 3.6 cm - 1.8 cm,
and 1.8 cm - 0.0 cm from the shear flow chamber (top view). Shear is
in the y-direction. Gas flow is from right to left. Helium velocity is 8.3
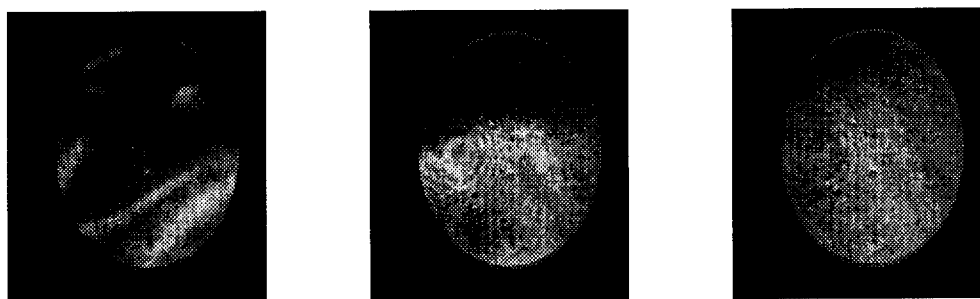m/sec. Nitrogen velocity is 1.5 m/sec.

Figure 52.   Camera 1,1 interference patterns for 5.4 cm - 3.6 cm, 3.6 cm - 1.8 cm, and 1.8 cm - 0.0 cm from the shear flow chamber (top view). Shear is in the y-direction. Gas flow is from right to left. Helium velocity is 8.3 m/sec. Nitrogen velocity is 1.5 m/sec.

Figure 53.   Camera 1,2 interference patterns for 5.4 cm - 3.6 cm, 3.6 cm - 1.8 cm, and 1.8 cm - 0.0 cm from the shear flow chamber (top view). Shear is in the y-direction. Gas flow is from right to left. Helium velocity is 8.3 m/sec. Nitrogen velocity is 1.5 m/sec.
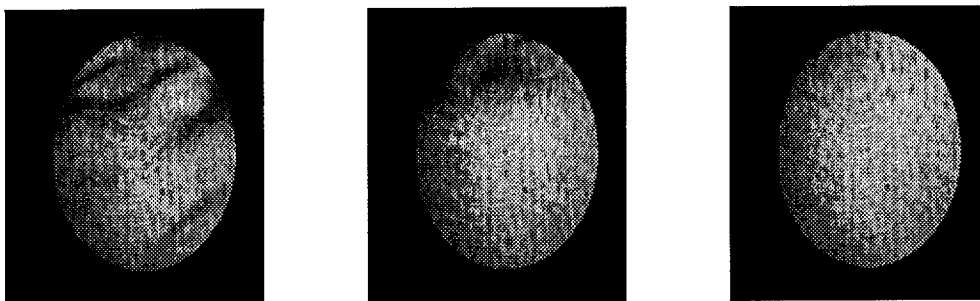

Figure 54.   Camera 0,0 interference patterns for 5.4 cm - 3.6 cm, 3.6 cm - 1.8 cm, and 1.8 cm - 0.0 cm from the shear flow chamber (top view). Shear is in the x-direction. Gas flow is from right to left. Helium velocity is 8.3 m/sec. Nitrogen velocity is 1.5 m/sec.
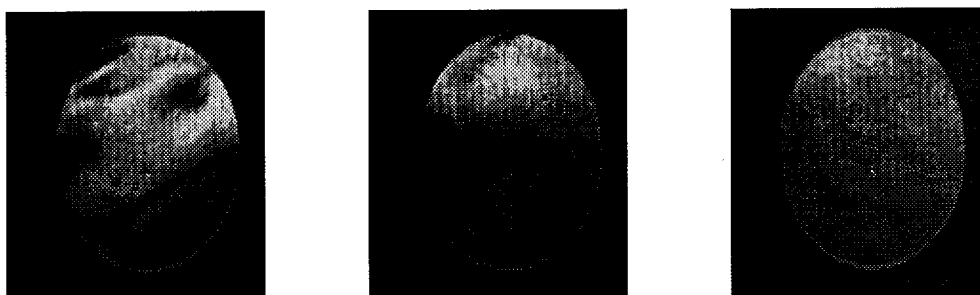
Figure 55. Camera 0,1 interference patterns for 5.4 cm - 3.6 cm, 3.6 cm - 1.8 cm, and 1.8 cm - 0.0 cm from the shear flow chamber (top view). Shear is in the x-direction. Gas flow is from right to left. Helium velocity is 8.3 m/sec. Nitrogen velocity is 1.5 m/sec.
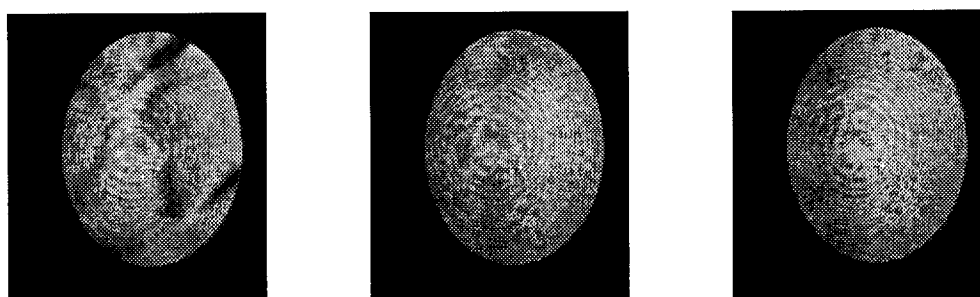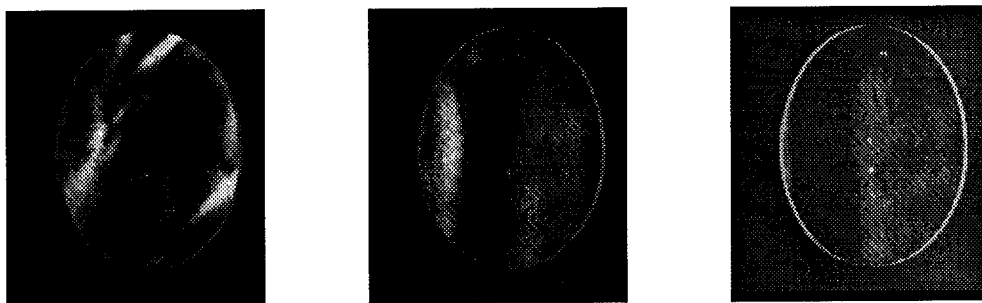

Figure 56. Camera 0,2 interference patterns for 5.4 cm - 3.6 cm, 3.6 cm - 1.8 cm, and 1.8 cm - 0.0 cm from the shear flow chamber (top view). Shear is in the x-direction. Gas flow is from right to left. Helium velocity is 8.3 m/sec. Nitrogen velocity is 1.5 m/sec.

Figure 57. x-direction interferogram patterns for 5.4 cm - 3.6 cm, 3.6 cm - 1.8 cm, and 1.8 cm - 0.0 cm from the shear flow chamber (top view). The fringe separation is proportional to the wavefront slope in the x direction. Gas flow is from right to left. Helium velocity is 8.3 m/sec. Nitrogen velocity is 1.5 m/sec.

Figure 58. y-direction interferogram patterns for 5.4 cm - 3.6 cm, 3.6 cm - 1.8 cm, and 1.8 cm - 0.0 cm from the shear flow chamber (top view). The fringe separation is proportional to the wavefront slope in the y direction. Gas flow is from right to left. Helium velocity is 8.3 m/sec. Nitrogen velocity is 1.5 m/sec.

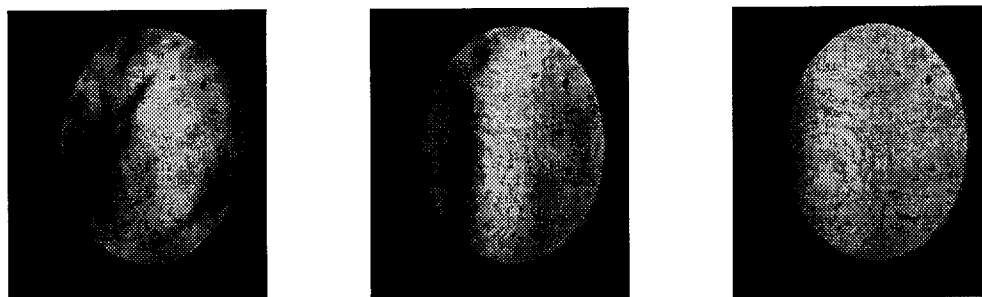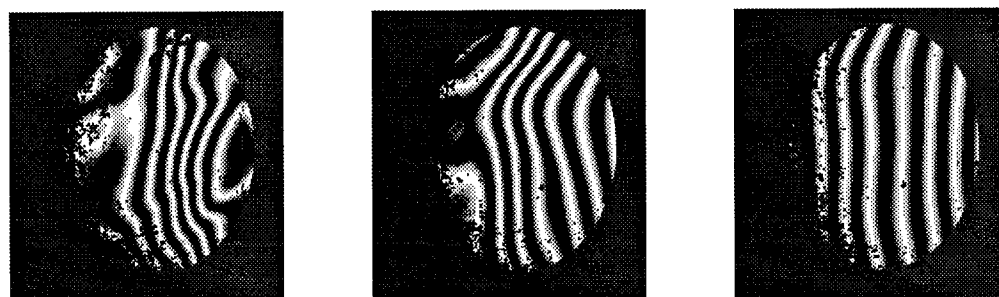Figure 59. Phase map for 1.8 cm - 0.0 cm from the shear flow chamber (top view). Gas flow is from right to left. Helium velocity is 8.3 m/sec. Nitrogen velocity is 1.5 m/sec. (The x axis in this figure corresponds to the y-direction)

Figure 60. Phase map for 3.6 cm - 1.8 cm from the shear flow chamber (top view). Gas flow is from right to left. Helium velocity is 8.3 m/sec. Nitrogen velocity is 1.5 m/sec. (The x axis in this figure corresponds to the y-direction)
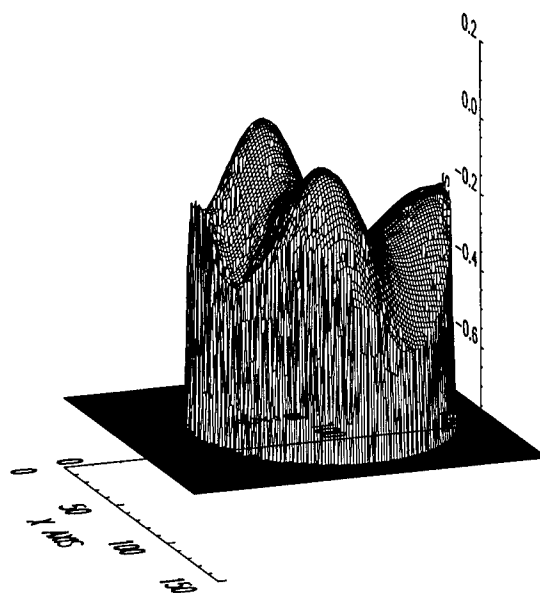

Figure 61. Phase map for 5.4 cm - 3.6 cm from the shear flow chamber (top view). Gas flow is from right to left. Helium velocity is 8.3 m/sec. Nitrogen velocity is 1.5 m/sec. (The x axis in this figure corresponds to the y-direction)
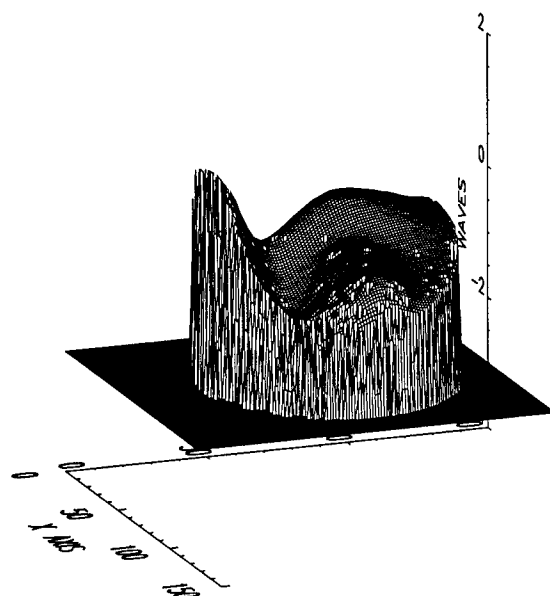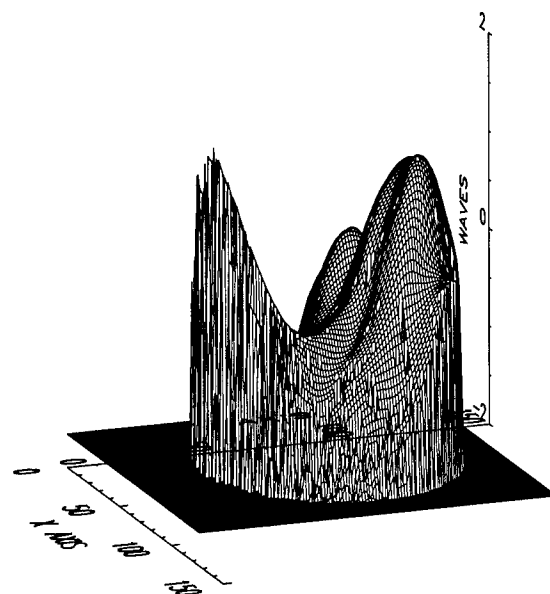
Bibliography

1. Chew, Larry and Walter Christiansen. "Coherent Structure Effects on the Optical Performance of Plane Shear Layers," *AIAA*, *29* (January 1991). pp. 76 - 80.

2. Hesslink, L. *Optical Tomography*, 124 - 131. Handbook of Flow Visualization, Hemisphere Publishing, New York, NY, 1989. Chap. 20.

3. Johnson, Robert L. *Numerical simulation of tomographic reconstruction for the study of turbulence using optical wavefront sensor measurements*. MS Thesis, AFIT/GAP/ENP/93D-04, Graduate School of Engineering, Air Force Institute of Technology (AETC), Wright-Patterson AFB OH, 1993.

4. Jumper, E. J. and R. J. Hugo. "Optical Phase Distortion Due to Turbulent-Fluid Density Fields: Quantification Using the Small-Aperture Beam Technique," *AIAA 23rd Plasmadynamics & Lasers Conference*, (92-3020) (July 1992).

5. Magee, Eric Parker. *Characterization of Laboratory Generated Turbulence by Optical Phase Measurements*. MS Thesis, AFIT/GEO/ENG/93M-03, Graduate School of Engineering, Air Force Institute of Technology (AETC), Wright-Patterson AFB OH, 1993.

6. Merzkirch, Wolfgang. *Flow Visualization* (Second Edition). Academic Press, Inc., 1987.

7. Pedersen, Bryon L. *Experimental verification of tomographic reconstruction of turbulent air flow structure using optical wavefront measurements*. MS Thesis, AFIT/GEO/ENG/93D-01, Graduate School of Engineering, Air Force Institute of Technology (AETC), Wright-Patterson AFB OH, 1993.

8. Roggemann, M. C. and B. M. Welsh. "Class Notes, EENG 716, Atmospheric Optics." School of Engineering, Air Force Institute of Technology, April 1994.

9. Sandler, D.G., et al. "Shearing interferometry for laser-guide-star atmospheric correction at large D/r_o," *J. Opt. Soc. Am. A*, *11*:858–873 (1994).

10. Serway, Raymond A. *Physics for scientists and engineers* (second Edition). Saunders College Publishing, 1986.

11. Sherikar, S. V. and R. Chevray. *Aerosol Formation in a Mixing Layer*, 124 - 131. Turbulent Shear Flows 3, Springer-Verlag, 1981.

12. Truman, C. Randall and Moon Joo Lee. "Effects of organized turbulence structures on the phase distortion in a coherent optical beam propogating through a turbulent shear flow," *Phys. Fluids A*, *2*(5):851 - 857 (May 1990).

13. Vennard, John K. and Robert L. Street. *Elementary Fluid Mechanics* (Fifth Edition). John Wiley & Sons, Inc.

14. Wallner, Edward P. "Optimal wave-front correction using slope measurements," *Optical Society of America, 73* (December 1983).

15. Wissler, John B. *Transmission of thin light beams through turbulent mixing layers.* PhD dissertation, California Institute of Technology, 1992.

Vita

First Lieutenant Daniel Warren Jewell was born on March 13,1961 in Warren, Pennsylvania. He graduated from Lawrence Central High School in Lawrence, Indiana in 1979 and joined the U.S. Air Force as a Computer Maintenance Technician. After his acceptance into the Airmans Education and Commissioning Program in 1987, he attended the University of Missouri-Rolla, Rolla, Missouri where he received a Bachelor of Science degree in Electrical Engineering in May 1990. Upon graduation, he entered Officer Training School and was commissioned a lieutenant in the United States Air Force. He served as a Satellite Systems Engineer at 6th Satellite Operations Squadron where he was responsible for the state-of-health and anomaly resolution of the Defense Meteorological Satellite Program weather satellites. In May 1993, he entered the School of Electrical Engineering, Air Force Institute of Technology.

Permanent address: 2855 College Hill Ct.
Beavercreek, OH 45324

REPORT DOCUMENTATION PAGE

1. AGENCY USE ONLY (Leave blank)	2. REPORT DATE December 1994	3. REPORT TYPE AND DATES COVERED Master's Thesis

4. TITLE AND SUBTITLE

Flow Visualization of a Turbulent Shear Flow using an
Optical Wavefront Sensor

5. FUNDING NUMBERS

6. AUTHOR(S)

Daniel W. Jewell, Captain, USAF

7. PERFORMING ORGANIZATION NAME(S) AND ADDRESS(ES)

Air Force Institute of Technology, WPAFB OH 45433-6583

8. PERFORMING ORGANIZATION REPORT NUMBER

AFIT/GEO/ENG/94D-04

9. SPONSORING / MONITORING AGENCY NAME(S) AND ADDRESS(ES)

Dr. Lenore McMackin
PL/LIMI
Kirtland AFB, NM 87117-6008

10. SPONSORING / MONITORING AGENCY REPORT NUMBER

11. SUPPLEMENTARY NOTES

12a. DISTRIBUTION / AVAILABILITY STATEMENT

Approved for public release; distribution unlimited

12b. DISTRIBUTION CODE

13. ABSTRACT (Maximum 200 words)

The research reported here investigated the use of a shearing interferometer (SI) wavefront sensor to determine the effects of shear-layer turbulence on an optical wavefront. A collimated helium-neon laser beam was propagated through a plane shear-layer produced by mixing helium and nitrogen at different velocities. Since the gases have different indices of refraction, the optical wavefront was distorted by different amounts by each gas. The SI measured the wavefront slope across the sampled area of the wavefront. The shear-layer was viewed from two orthogonal directions. This document contains shadowgraphs, interference patterns imaged by each of the SI's six cameras, interferograms containing fringes with separation proportional to the wavefront slope, and phase maps showing the shape of the perturbed optical wavefronts. The side view showed an area of steep slope along the mixing area of the two gases. The slope gradually changed as the distance from the mixing layer region increased. For the top view, the peaks and valleys grew as they propagated away from the shear-layer turbulence generator. The results also indicated that the interference patterns recorded by the SI cameras provide a simple way to visualize turbulence in a manner that provides phase information about the wavefront.

14. SUBJECT TERMS

Flow visualization, shear flow, shear layer, SI, shearing interferometer, optical wavefront sensor, shadowgraph, turbulence, Helium, Nitrogen

15. NUMBER OF PAGES

67

16. PRICE CODE

17. SECURITY CLASSIFICATION OF REPORT	18. SECURITY CLASSIFICATION OF THIS PAGE	19. SECURITY CLASSIFICATION OF ABSTRACT	20. LIMITATION OF ABSTRACT
Unclassified	Unclassifed	Unclassified	UL

GENERAL INSTRUCTIONS FOR COMPLETING SF 298

The Report Documentation Page (RDP) is used in announcing and cataloging reports. It is important that this information be consistent with the rest of the report, particularly the cover and title page. Instructions for filling in each block of the form follow. It is important to *stay within the lines* to meet *optical scanning requirements.*

Block 1. Agency Use Only *(Leave blank)*.

Block 2. Report Date. Full publication date including day, month, and year, if available (e.g. 1 Jan 88). Must cite at least the year.

Block 3. Type of Report and Dates Covered. State whether report is interim, final, etc. If applicable, enter inclusive report dates (e.g. 10 Jun 87 - 30 Jun 88).

Block 4. Title and Subtitle. A title is taken from the part of the report that provides the most meaningful and complete information. When a report is prepared in more than one volume, repeat the primary title, add volume number, and include subtitle for the specific volume. On classified documents enter the title classification in parentheses.

Block 5. Funding Numbers. To include contract and grant numbers; may include program element number(s), project number(s), task number(s), and work unit number(s). Use the following labels:

C	- Contract	PE	- Project
G	- Grant	TA	- Task
PE	- Program Element	WU	- Work Unit Accession No.

Block 6. Author(s). Name(s) of person(s) responsible for writing the report, performing the research, or credited with the content of the report. If editor or compiler, this should follow the name(s).

Block 7. Performing Organization Name(s) and Address(es). Self-explanatory.

Block 8. Performing Organization Report Number. Enter the unique alphanumeric report number(s) assigned by the organization performing the report.

Block 9. Sponsoring/Monitoring Agency Name(s) and Address(es). Self-explanatory.

Block 10. Sponsoring/Monitoring Agency Report Number. *(If known)*

Block 11. Supplementary Notes. Enter information not included elsewhere such as: Prepared in cooperation with...; Trans. of...; To be published in.... When a report is revised, include a statement whether the new report supersedes or supplements the older report.

Block 12a. Distribution/Availability Statement. Denotes public availability or limitations. Cite any availability to the public. Enter additional limitations or special markings in all capitals (e.g. NOFORN, REL, ITAR).

DOD - See DoDD 5230.24, "Distribution Statements on Technical Documents."
DOE - See authorities.
NASA - See Handbook NHB 2200.2.
NTIS - Leave blank.

Block 12b. Distribution Code.

DOD - Leave blank.
DOE - Enter DOE distribution categories from the Standard Distribution for Unclassified Scientific and Technical Reports.
NASA - Leave blank.
NTIS - Leave blank.

Block 13. Abstract. Include a brief *(Maximum 200 words)* factual summary of the most significant information contained in the report.

Block 14. Subject Terms. Keywords or phrases identifying major subjects in the report.

Block 15. Number of Pages. Enter the total number of pages.

Block 16. Price Code. Enter appropriate price code *(NTIS only)*.

Blocks 17. - 19. Security Classifications. Self-explanatory. Enter U.S. Security Classification in accordance with U.S. Security Regulations (i.e., UNCLASSIFIED). If form contains classified information, stamp classification on the top and bottom of the page.

Block 20. Limitation of Abstract. This block must be completed to assign a limitation to the abstract. Enter either UL (unlimited) or SAR (same as report). An entry in this block is necessary if the abstract is to be limited. If blank, the abstract is assumed to be unlimited.